

Driving high capacity anode-free lithium metal batteries under unpressurized and lean electrolyte condition by an electron-deficient current collector

Hyeokjin Kwon

Korea Advanced Institute of Science and Technology

Ju-Hyuk Lee

Korea Advanced Institute of Science and Technology

Youngil Roh

Korea Advanced Institute of Science and Technology

Jaewon Baek

Korea Advanced Institute of Science and Technology

Dong Jae Shin

Korea Advanced Institute of Science and Technology

Jong Keon Yoon

LG Energy Solution

Hoe Jin Ha

LG Energy Solution

Je Young Kim

LG Energy Solution

Hee-Tak Kim (✉ heetak.kim@kaist.ac.kr)

Korea Advanced Institute of Science and Technology <https://orcid.org/0000-0003-4578-5422>

Article

Keywords: Long-term Cycling, Liquid Electrolyte, Solid Electrolyte Interphase, Nano-window, Electron Tunneling, Defect Chemistry

Posted Date: March 1st, 2021

DOI: <https://doi.org/10.21203/rs.3.rs-135585/v1>

License:   This work is licensed under a Creative Commons Attribution 4.0 International License.

[Read Full License](#)

Version of Record: A version of this preprint was published at Nature Communications on September 20th, 2021. See the published version at <https://doi.org/10.1038/s41467-021-25848-1>.

1 **Driving high capacity anode-free lithium metal batteries under unpressurized and lean**
2 **electrolyte condition by an electron-deficient current collector**

3

4 **Abstract:** The long-term cycling of anode-free lithium metal batteries (AF-LMBs) with a
5 liquid electrolyte is hindered by the formation of inhomogeneous solid electrolyte interphase
6 (SEI) on current collector and the subsequent irregular Li deposition. Here, we report the nano-
7 window (NW) defect-enriched carbon current collector with a lowered Fermi level, which can
8 address the critical issues. The low Fermi-level surface induces a defect-free SEI layer by
9 alleviating electron tunneling at the interface, and leads to high Li nucleation density and lateral
10 Li growth via Li-C orbital hybridization. DFT calculations and spectroscopic analyses
11 elucidate that these effects are rooted in the electron deficiency of the NW defect structure. An
12 AF-LMB employing an NCM811 cathode, NW-enriched 3D-current collector, and carbonate
13 liquid electrolyte exhibits 90% capacity retention for over 50 cycles under unpressurized and
14 lean electrolyte conditions. The defect chemistry presents a new design principle of tuning the
15 electronic structure of current collectors enabling 3-dimensional Li deposition in AF-LMBs.

16 **Main Text:**

17 **Introduction**

18 To achieve high energy density lithium (Li) metal batteries, a limited negative to positive
19 capacity ratio, a low electrolyte amount to capacity (E/C) ratio, and a high loading cathode are
20 considered to be requisite conditions. In this aspect, an anode-free Li metal battery (AF-LMB)
21 featuring no Li metal in its initial state is the ultimate version of LMB technology¹⁻⁴. During
22 the first charging of an AF-LMB, a Li metal is electroplated on the anode current collector.
23 However, the Li/current collector interface in the AF-LMB presents critical challenges, which
24 include cathodic Li corrosion⁵ and ramified Li electrodeposition on the current collector^{6,7}.
25 Like other types of LMBs, the uncontrolled reaction between the roughened Li deposit and
26 electrolyte critically limits the long-term cycling of the AF-LMB. It becomes severe at high
27 cathode loading and a low E/C ratio, hindering augmentation of energy density.

28 Considerable efforts have recently been made to control Li plating/stripping on the current
29 collector, including the use of various host materials⁸⁻¹², a coherent lattice¹³, and an increase of
30 temperature or pressure^{2,14-18}. While the efficacy of three dimensional (3D) porous current
31 collectors in reducing the effective current density has been proven, their enlarged electroactive
32 surface area can accompany a larger degree of electrolyte decomposition. Furthermore,
33 external cell pressurization, which is known to mitigate the inhomogeneous Li
34 electrodeposition, is not compatible with 3D current collectors.

35 Regarding the cycling life of AF-LMBs, the initial structure and the properties of the SEI
36 formed on the current collector are highly important, because they influence the sequential
37 evolution of the Li deposit morphology from electrochemical and mechanical aspects^{19,20}. The
38 mosaic and grain-coalesced SEI formed on the current collector, which originates from
39 aggressive electron tunneling from the current collector to the electrolyte, induces uneven Li
40 nucleation, resulting in protrusion of the Li deposit through the defects in the SEI. Electrolyte

41 design has been a major strategy to control the structure of the SEI in the AF-LMB; however,
42 we envisioned that lowering Fermi level at the surface of the current collector can enfeeble the
43 electron tunneling by increasing the tunneling barrier. Considering the recently reported
44 cathodic corrosion of Li due to the electron transfer from the current collector to the electrolyte⁵,
45 a properly-tuned electronic structure is of significant interest in terminating the interfacial
46 electron transfer. Furthermore, a low Fermi level surface can provide a means to control the Li
47 nucleation and growth mode on the current collector based on the electronic interaction
48 between electropositive Li and the electron-deficient current collector.

49 With the concept of tuning the electronic structure of the current collector, we present a
50 nano-window (NW) defect (a high degree vacancy defect)-enriched carbon surface as an
51 anode current collector of AF-LMBs. In contrast to the non-uniform SEI formation and
52 dendritic Li growth on the graphite surface, the NW structure addresses the critical issues at
53 the anode interface by 1) forming a thin and uniform SEI and 2) promoting high Li nucleation
54 density and lateral Li growth on its surface. The excellent interfacial compatibility of the NW
55 with the AF-LMB design originates from its low Fermi level property, which can suppress
56 electron tunneling to the LUMO level of the electrolyte, and impart strong binding of Li
57 adatoms via orbital hybridization (electron transfer) (Fig. 1). The defect-free SEI and Li-C
58 orbital hybridization enable lateral Li deposition even in the internal structure of the 3D
59 current collector where no external pressure is exerted normal on its surfaces. We report that
60 an AF-LMB with the NW defect-enriched 3D current collector has an unprecedented
61 capacity retention of 90% at 50 cycles without pressurized electrodeposition or elevated
62 temperature at high current density (2 mA cm^{-2}), high areal capacity (4.2 mAh cm^{-2} of
63 NMC811), and a lean carbonate electrolyte condition (E/C ratio of $4.0 \mu\text{l mAh}^{-1}$). This paper
64 confirms the possibility of the tuning of the SEI structure on the current collector by
65 designing the electronic structure of the surface, and presents an understanding of lithiophilic

66 current collectors based on orbital hybridization between Li and the electron-deficient
67 surface.
68

69 **NW defect-enriched carbon surface on 3D carbon fiber current collector**

70 We chose a carbon layer with high density-vacancy defects as an electron deficient current
71 collector. The defect structure was formed on the graphitic surface of a commercial carbon
72 paper by coating and subsequent carbonization of a zeolitic imidazole framework (ZIF-8). ZIF-
73 8 can be converted to a highly defective carbon structure by heating due to the evaporation of
74 Zn and N atoms^{21,22}. The pristine carbon paper (p-CP) and defective carbon layer-coated carbon
75 paper (d-CP) enable a focused comparison of graphitic and defective surfaces excluding the
76 effect of the geometry of the current collector.

77 The structures of p-CP, ZIF-8 coated p-CP (ZIF-8@p-CP), and d-CP were investigated by
78 using scanning electron microscopy (SEM), X-ray photoelectron spectroscopy (XPS), and
79 energy-dispersive X-ray spectroscopy (EDX) mapping. As shown in Figs. 2a and b, the
80 diameter of the carbon fiber was around 6.0 μm , and the scale of the interstitial space between
81 adjacent fibers was tens of microns. The SEM images of ZIF-8@p-CP (Supplementary Fig. 1a)
82 show that crystalline ZIF-8 particles covered the carbon fibers of p-CP. The Zn, N, and O
83 signals in the XPS survey spectra and EDX mapping of p-CP, ZIF-8@p-CP, and d-CP confirm
84 the surface decoration of ZIF-8 and the carbonization of ZIF-8 (Supplementary Figs. 1b-f and
85 Supplementary Table 1). The XPS survey spectrum of d-CP shows a very low N content of
86 1.2 % for d-CP with no signal of the Zn element (Supplementary Fig. 1c), indicating the
87 removal of N and Zn from ZIF by the carbonization process^{21,22}. During the carbonization
88 process, the locally grown ZIF-8 nanocrystals laterally spread along the carbon fiber surfaces
89 due to the structural collapse of ZIF-8^{23,24}, resulting in a webby carbon layer on the surface, as
90 shown in Figs. 2c and d.

91 The high-resolution transmission electron microscope (HR-TEM) analysis with
92 corresponding fast Fourier transform (FFT) revealed the difference in the basal plane
93 crystallinity between p-CP and d-CP (Figs. 2e, f). The HR-TEM images of p-CP featuring

94 hexagonally packed carbon atoms with 2.46 Å nearest-neighbor hexagon center separation
95 verified its highly crystalline structure²⁵. The corresponding FFT analysis revealed the
96 hexagonal shaped reciprocal-space pattern, demonstrating a sp² hybridized graphene surface.
97 In contrast, d-CP showed a disordered basal plane structure in its HR-TEM image together with
98 a diffusion halo in its FFT image, which is characteristic of a disordered structure. The bonding
99 structures of the p-CP and d-CP surface were quantitatively analyzed by XPS (Fig. 2g). A
100 pronounced difference between the two electrodes is that the peak at 283.7 eV in C1s spectra
101 corresponding to a vacancy defect^{26,27} was much larger for d-CP. The peak intensity ratio of
102 vacancy to sp² hybridized carbon was 0.175 for p-CP and 0.403 for d-CP. The defective
103 structure of d-CP was also confirmed by the Raman spectra of p-CP and d-CP (Fig. 2h). The
104 ratio of D (1330-1340 cm⁻¹) and G (1590-1600 cm⁻¹) bands (I_D/I_G), which is indicative of defect
105 density, was 1.240 for p-CP and 1.744 for d-CP, indicating a vacancy-rich defective carbon
106 surface of d-CP. The ratio of the 2D-band around 2700 cm⁻¹ and the G band was lower than
107 unity (0.496 for p-CP and 0.603 for d-CP), reflecting the formation of defects on the layered
108 structure²⁸⁻³⁰.

109 The pore structure of the defective layer was analyzed by nitrogen adsorption isotherm (BET
110 isotherm) and Barrett-Joyner-Halenda (BJH) pore size distribution analyses (Fig. 2i,
111 Supplementary Fig. 2a-d). The isotherm of d-CP featuring a concave-shaped quantity-
112 adsorbed-curve at the low relative pressure region is a general characteristic of micropores (<
113 2 nm). In the BJH pore size distribution analysis, d-CP exhibited an intensive signal at 1.2 nm
114 and a weaker signal at 0.9 nm, which correspond to 8 and 6 missing carbons, respectively.
115 Based on the spectroscopic and pore size analysis, d-CP can be characterized as an NW-
116 enriched surface, as shown in Fig. 2j.

117 **Defect-free SEI formation at the defective current collector-electrolyte interface**

118 The decomposition of the electrolyte on the anode current collector accompanies the
119 evolution of the SEI. Because the structure of the SEI on the current collector plays a critical
120 role in guiding subsequent Li electrodeposition in the AF-LMB system, the microstructure of
121 the initial SEI on the current collector should be controlled. In addition, because the
122 consumption of electrolyte to form the SEI increases linearly with the surface area of the
123 electrode, the current collectors with expanded surface area such as in the case of a 3D current
124 collector are hardly employed for AF-LMBs in spite of their advantage of lowering the
125 effective current density for uniform Li deposition. Therefore, we sought to design a current
126 collector/electrolyte interface that generates a uniform SEI microstructure and suppresses the
127 electrolyte decomposition.

128 Figure 3a shows the first cycle voltage profile of p-CP and d-CP for a galvanostatic reduction
129 down to 0.0 V and subsequent oxidation up to 2.0 V. As an electrolyte, 1 M LiPF₆ ethylene
130 carbonate (EC)/diethyl carbonate (DEC) (1/1 in volume) with 10 wt% fluoroethylene carbonate
131 (FEC) and 1 wt% vinylene carbonate (VC) was used. The similar lithiation capacity of p-CP
132 and d-CP indicates that introduced defect layer has little effect on the reversible graphite
133 capacity. In this potential window of 0 V-2.0 V, Li metal deposition does not occur, thus the
134 irreversible capacity originates from electrolyte decomposition and consequent SEI generation
135 on each current collector. The initial Coulombic efficiency (CE) for d-CP was 87.4 %, which
136 is higher than that of p-CP (80.8 %), in spite of its much larger electroactive surface area
137 (Supplementary Fig. 2). According to a linear sweep voltammetry (LSV) (Fig. 3b), d-CP also
138 exhibited much lowered reduction current per electroactive surface area from electrolyte
139 decomposition, demonstrating that the surface of d-CP is less active for the reduction of the
140 electrolyte. The result is antithetical to previous perceptions that the irreversible capacity from

141 SEI formation is nearly proportional to the specific area of electrode material and that a
142 defective atomic structure of carbon promotes copious SEI formation^{20,31,32}.

143 The structure of the SEI formed on p-CP and d-CP current collector according to the charge
144 voltage cut-off was analyzed through XPS. The composition of the inner SEI was observed
145 after charging up to 1.0 V and the outer SEI after charging up to 0.0 V. As shown in Fig. 3c,
146 p-CP exhibited strong potential dependency of SEI composition: with lowering the cut-off
147 voltage, the intensities of LiF, Li₂CO₃ decreased and the intensity of C-O, C=O (components
148 for lithium alkyl carbonate, R-OCO₂Li) and Li₂O increased, indicating a disparity of the SEI
149 composition between the inorganic-rich inner and organic-rich outer SEI, consistent with a
150 typical multilayer SEI model^{20,33}. By sharp contrast, for d-CP (Fig. 3d), the XPS spectra for
151 two different cut-off voltages were nearly identical, exhibiting Li₂CO₃ and LiF-rich structure.
152 This indicates that the early formed SEI on d-CP effectively suppressed further electrolyte
153 decomposition. The F1s spectra at 1.0 V demonstrates the formation of LiF for both p-CP and
154 d-CP. However, for the cut-off voltage of 0.0 V, strong signals of Li_xPO_yF_z and LiP_xF_y,
155 indicative of the decomposition of PF₆⁻, newly appeared for p-CP in contrast to the weak
156 Li_xPO_yF_z and LiP_xF_y signal observed for d-CP. The XPS analysis suggests the chemical
157 structures of SEI on p-CP and d-CP, as illustrated in Fig. 3e.

158 To investigate the thickness and microstructure of SEI, a TEM analysis was performed (Fig.
159 3f-i). The thickness of SEI on d-CP (17.3 nm) was about one-third of that on p-CP (~50 nm),
160 verifying that the SEI formation by electrolyte decomposition was suppressed on d-CP. A
161 closer look at the SEIs in Figs. 3g and i reveals that the SEI on p-CP has an irregular mosaic
162 SEI structure and randomly dispersed organic and inorganic grains (indicated by orange
163 circles), whereas d-CP has a uniform SEI structure. Considering that the mosaic structure
164 originates from successive decomposition of different electrolyte components at different
165 potentials, the thin and uniform SEI on d-CP suggests self-limiting of SEI formation at the

166 early stage of electrolyte decomposition. In particular, the SEI on d-CP shows a homogeneous
167 structure without any observable crystalline domains larger than a few nanometers. Based on
168 the high self-limiting property of SEI formation on d-CP, we presumed that SEI components
169 are formed sporadically without growth of organic or inorganic grains, resulting in a uniform
170 SEI structure rather than a grain coalesced mosaic structure. The high uniformity of the SEI on
171 d-CP can facilitate uniform Li^+ flux and diminish focused Li nucleation, which are
172 requirements for uniform Li nucleation and growth (Figs. 3j, k).

173 **Alleviated electron tunneling on electron deficient defect structure**

174 To gain insight into the mechanism of thin and uniform SEI formation on d-CP, we
175 investigated the change of atomic and electronic structures of p-CP and d-CP during the initial
176 lithiation before lithium metal deposition. Fig. 4a compares the potential profiles in the voltage
177 range from OCV to 0.8 V for p-CP and d-CP. A larger capacity in the potential window was
178 observed for d-CP than p-CP. A distinguished potential plateau at 1.2 V observed for p-CP
179 corresponds to the decomposition potential of FEC. In order to trace the variation of the
180 electronic structure during the early stage lithiation, the work function (WF), which is the
181 difference between the vacuum level (E_{vac}) and Fermi level, was measured along the potential
182 descending for p-CP and d-CP by using UV photoelectron spectroscopy (UPS, Supplementary
183 Fig. 3). As described in Figure 4b, the work function of the surface of p-CP is 4.52 eV, which
184 is coincident with the work function of the graphite reported in previous studies³⁴, and that of
185 d-CP is 4.80 eV. Fermi levels of p-CP and d-CP increased with decreasing potential upon
186 lithiation. Notably, Fermi levels of d-CP were much lower than those of p-CP, exhibiting a
187 difference of 0.22 - 0.59 eV, indicating that the surface of d-CP has a lower electron energy
188 level.

189 The structural changes of p-CP and d-CP in the potential range were traced by an operando
190 X-ray diffraction (XRD) analysis (Fig. 4c, d). The XRD image plots in the 24-30° region shed
191 light on the lithiation process of the graphitic structure of carbon fiber. In contrast to the strong
192 peak at 2θ of 26.5° from G(002) of p-CP, the weak intensities at around 26.5° for d-CP indicate
193 the existence of a defective carbon layer. For d-CP, the lithiated structures of LiC_6 and LiC_{12}
194 started to appear at lower lithiation capacities than for p-CP, suggesting that fast Li transport
195 through the defective layer facilitates the lithiation of the inner graphitic carbon fiber. The
196 structural evolution of the defect structure can be traced from the higher 2θ region. From the
197 beginning of the lithiation, a peak at $2\theta=43^\circ$ appeared for d-CP and gradually grew with

198 decreasing potential, indicating Li insertion in the NW defect structure of the graphite
199 surface^{35,36}. The structural change of d-CP indicates that the larger capacity during the early
200 lithiation and lower Fermi levels for d-CP originate from the lithiated structure of the NW. By
201 contrast, the XRD pattern of p-CP was invariant in the potential range. This suggests that the
202 Fermi level change of p-CP is attributed to solid-solution type lithiation at the 1L stage of initial
203 graphite lithiation (Li_xC_6 , $x < 0.16$)^{37,38}, which does not change the lattice structure of graphite.

204 To further understand the lower Fermi levels of d-CP, we calculated the atomistic
205 (Supplementary Fig. 4) and electronic structure (Fig. 4e) for the NW in bilayer graphene (BLG)
206 in comparison with perfect BLG. With the introduction of the NW defect to BLG, it moves
207 toward valence bands, similar to p-type doping³⁹⁻⁴¹, due to the electron-deficient property of
208 the NW. As a result, the Fermi level of the NW structure (-5.11 eV) is much lower than that of
209 perfect BLGs (-4.62 eV) (Fig. 4f, Supplementary Fig. 5). According to the calculations of the
210 sequential lithiation process, a Li atom spontaneously penetrates through the NW hole,
211 accepting electrons of Li by the electron-deficient NW (Supplementary Fig. 6, 7) and places
212 between the graphene layers with a gradual diminution of spin momentum (Supplementary Fig.
213 8, 9) until a stoichiometry of Li_3C_8 (fully lithiated state) is reached (Fig. 4g). The calculated
214 electric potentials and Fermi levels of Li-NW structures at different degrees of lithiation are
215 shown in Fig. 4h. The potential change with lithiation accounts for the larger lithiation capacity
216 of d-CP above 1.5 V vs. Li/Li^+ . In accordance with the UPS results, the Fermi level of the NW
217 structure is increased with lithiation, because it shifts toward the conduction band
218 (Supplementary Fig. 7). The results of the calculation state that although the lithiation is
219 proceeded, the Fermi level of d-CP is still lower than that of p-CP at each potential thanks to
220 the electron-deficient NW structure that can lower electron energy receiving electrons from Li.

221 Based on tunneling theory in quantum mechanics, the disparity of SEI thickness between p-
 222 CP and d-CP can be understood. The electron insulating property of the SEI depends on the
 223 SEI layer thickness (d) and Fermi level (E_f), as given in Eq. (1):³¹

$$T = \frac{16E_f\Delta E_t}{(E_f + \Delta E_t)^2} e^{-\frac{4\pi d}{h}\sqrt{2m\Delta E_t}} \quad (1)$$

224 where T is the electron tunneling probability for complete electron insulating (practically $T =$
 225 e^{-40})^{20,31}, E_f is the Fermi level of the electrode surface ($E_{vac} - \Phi_{\text{electrode}}$, $\Phi_{\text{electrode}}$ is the
 226 work function), ΔE_t is the electron tunneling barrier (energy difference between conduction
 227 band minimum of the SEI layer ($E_{CBM,SEI}$) and E_f), m is the mass of electron, and h is Planck's
 228 constant. Eq. (1) can be simplified as $T \sim e^{-d\sqrt{\Delta E_t}}$ by Wentzel-Kramers-Brillouin
 229 approximation in quantum tunneling theory³¹. Since ΔE_t increases with decrement of E_f , d-
 230 CP with a lower E_f can reach electro-insulation at a smaller d . Therefore, the electron-
 231 deficient NW surfaces can alleviate electrolyte decomposition and limit SEI growth at initial
 232 lithiation.

233 **Uniform Li deposition triggered by NW defect**

234 Uniform Li deposition is a prerequisite for a high performance AF-LMB. The fully lithiated
235 NW structure (Li-NW) can act as an efficient nucleation site due to its lithiophilic nature. We
236 investigated the morphological evolution of Li nuclei formed on p-CP and d-CP at 1.0 mA cm^{-2} .
237 For p-CP, Li nuclei were sparsely populated (Fig. 5a) and they grew normal to the surface
238 (Fig. 5b). The distribution of Li nuclei on p-CP would be determined by irregular Li^+ flux in
239 the defect-rich SEI or grain boundaries of the basal plane with higher surface energy⁴². With
240 further Li deposition (Fig. 5c), Li nuclei clustered, suggesting surface diffusion of Li adatoms
241 or nuclei on the low energy graphene surface and their coalescence by van der Waals
242 interaction⁴³⁻⁴⁵. A focused investigation of a Li cluster (Fig. 5g) revealed that the agglomerated
243 Li nuclei have poor regularity of the lattice structure in the TEM image, scanning transmission
244 electron microscopy (STEM), and the pattern of rings in the FFT images. The aggregative
245 growth behavior corresponds to Volmer-Weber growth mode, which depicts a situation where
246 metal to metal interaction is stronger than metal to substrate interaction^{46,47}.

247 In sharp contrast, for d-CP, Li nuclei were densely populated and homogeneously distributed
248 on their surface (Figs. 5d, e), which suggests that the defect-free SEI provides uniform Li^+ flux
249 to the electrode surface^{19,48} and the Li-NW structure acts as a favorable nucleation site. Further
250 Li deposition led to lateral growth of nuclei and merging of nearby nuclei to form a planar Li
251 deposit (Fig. 5f). This implies that metal to substrate interaction is stronger than metal to metal
252 interaction, which corresponds to the Frank-van der merwe growth mode⁴⁷. According to the
253 TEM, STEM, and FFT analyses (Fig. 5h), the Li nuclei formed on d-CP had a monocrystalline
254 surface facet, which confirms the prevention of surface diffusion and aggregation of Li nuclei
255 by Li-NW structures.

256 The electrochemical analysis further confirms the distinguished Li nucleation/growth
257 behaviors between p-CP and d-CP. As shown in Supplementary Fig. 10, the Li nucleation

258 behaviors can be successfully analyzed by the Scharifker and Hills theory. For p-CP and d-CP,
259 the Li deposition processes showed an instantaneous nucleation mode. The nuclei number
260 densities calculated from the CA data were almost two orders of magnitude higher for those
261 for d-CP than that for p-CP (Supplementary Fig. 10c), which is consistent with the SEM
262 observation of Figs. 5a-f.

263 To obtain an understanding of uniform Li deposition on d-CP, we performed a DFT analysis
264 for electronic properties including partial density of states (pDOS) (Fig. 5i and Supplementary
265 Fig. 11), partial charge distribution (Supplementary Fig. 12), and adsorption energies of the Li
266 adatom. In Fig. 5i, the relaxed structures and pDOS spectra of single Li adsorbed on perfect
267 BLG, Li-NW, and Li-NW with four pre-adsorbed Li atoms are provided. The DOS spectra of
268 Li atoms on perfect BLG feature sharp pDOS of Li *s* and *p* orbitals. The DOS of C *s* and *p*
269 orbitals of perfect BLG are invariant with Li adsorption (Supplementary Fig. 5a and
270 Supplementary Fig. 11a). The results indicate the absence of electron transfer between BLG
271 and Li. By contrast, for Li atoms on Li-NW, broadening of DOS of Li and C *s* and *p* was
272 observed, indicating a hybridization of Li orbitals with C orbitals by electron transfer from the
273 electropositive Li atoms to electron deficient Li-NW (Supplementary Fig. 11b-d). In the same
274 vein, the partial charge distribution of Li adatoms and carbon atoms of the edge of the NW
275 defect also support electron transfer between them (Supplementary Fig. 12). Therefore, the
276 facile Li nucleation on d-CP is attributed to the strong orbital hybridization between Li and the
277 Li-NW. The arrangement of clusters of Li adatoms on BLG and Li-NW shown in Fig. 5j and
278 k supports the propensity of lateral Li growth for d-CP and vertical Li growth for p-CP. The
279 successively adsorbed five Li atoms on d-CP are distributed laterally on the Li-NW structure,
280 whereas they exhibited vertical aggregation on the BLG surface.

281 The comparison of the binding energy of Li atom on various atomic structures explains the
282 strong Li to substrate interaction for d-CP (Fig. 5l). The binding energy was highest on Li (111)

283 (1.89 eV) among various Li facets, which is identical to previous studies^{43,49,50}. The binding
284 energy for BLG was 1.73 eV, which is a lower value than that for Li (111), supporting the
285 Volmer-Weber growth mode for p-CP. However, the binding energy for the center of the Li-
286 NW was 3.13 eV, which is larger than those for any Li facets, which is in good agreement with
287 the Frank-van der merwe growth mode observed for d-CP. Also, the adsorption energy at the
288 center of NW defect is much larger than that when the Li atoms are located surrounding the
289 NW defect (Supplementary Fig. 13), explaining the hindered surface diffusion of Li nuclei for
290 d-CP.

291 **Cycling stability of the 3D carbon current collector with NW defect**

292 We investigated the reversibility of Li plating/stripping for Cu, p-CP, and d-CP with the
293 conventional carbonate electrolyte (1 M LiPF₆ EC/DEC+10% FEC+1% VC). Fig. 6a compares
294 the CEs of Li||Cu, Li||p-CP, and Li||d-CP half cells during the cycling at 2.0 mA cm⁻² and 5.0
295 mAh cm⁻². The voltage profiles during the cycling are shown in Supplementary Figs. 14a-c.
296 2D Cu and 3D p-CP were compared to assess the influence of reduced effective current density
297 due to the use of 3D structure. The Li||Cu cell showed an abrupt drop of CE at around 20 cycles
298 with an average CE of 93%. The cell failure was attributed to the formation of a localized thick
299 porous layer (Supplementary Figs. 14d, e). The Li||p-CP cell operated for 60 cycles with a 92.1%
300 average CE, indicating an improved cycling performance compared with the 2D Cu current
301 collector. However, from the post mortem analysis, the formation of a dead Li layer on p-CP
302 was observed similar to Cu (Supplementary Figs. 14f, g). The Li||d-CP cell exhibited high
303 cycling stability over 170 cycles with 98.6% CE. There have been few reports of a high CE
304 value and cyclic stability at the highly curtailed capacity of 5.0 mAh cm⁻² in carbonate
305 electrolyte-based half-cell (Supplementary Table 2). Contrary to the Li||Cu and Li||p-CP cells,
306 the cell failure of Li||d-CP was not caused by the d-CP electrode but by the depletion of the Li
307 metal counter electrode; the disassembled Li||d-CP cell after the cell failure showed depletion
308 of Li at the counter electrode and preservation of the porous structure in d-CP without the thick
309 dead Li layer (Supplementary Figs. 14h, i). A rate capability test for p-CP and d-CP
310 (Supplementary Fig. 14j) shows that d-CP can stably operate at 14 mA cm⁻² in contrast with
311 the rapid capacity fade with cycling for p-CP above 10 mA cm⁻².

312 As another measure of the reversibility of Li electrode, a Li||Li symmetric cell was
313 constructed with the Li-electroplated current collectors; Li was electrodeposited respectively
314 on Cu, p-CP, and d-CP at 0.2 mA cm⁻² and at 8 mAh cm⁻². The symmetric cells were cycled at
315 2 mA cm⁻² and at a Li utilization of 25% (2 mAh cm⁻²). As provided in Supplementary Fig. 15,

316 the d-CP symmetric cell maintained its smallest overpotential for more than 400 cycles, while
317 the Cu and p-CP cells showed irregular voltage spikes at 45 cycles and 42 cycles, respectively.
318 Consistent with the uniform nucleation of Li on Li-NW, the d-CP cell showed the lowest
319 deposition overpotential of 15 mV, being lower than the Cu cell value of 55 mV and p-CP cell
320 value of 28 mV.

321 The evolution of Li morphology during Li electrodeposition at 1.0 mA cm^{-2} with the
322 carbonate electrolyte was observed for p-CP and d-CP. Figs. 6b-i show SEM images of p-CP
323 at various Li deposition capacities (3, 5, 7, 9 mAh cm^{-2}). Localized protrusion of Li at the
324 surface of p-CP found at 3 mAh cm^{-2} triggered suffusion of the Li deposit on the top surface
325 of p-CP at larger deposition capacities. This indicates that the top Li deposition prevents the
326 utilization of the inner 3D structure of p-CP (Supplementary Fig. 14k). By sharp contrast, for
327 d-CP, its carbon fibers were uniformly covered by plated Li at 3 mAh cm^{-2} due to the uniform
328 Li nucleation and lateral growth driven by the NW structure (Fig. 6f). Further deposition led to
329 connection of the Li deposits to those on adjacent fibers (Fig. 6g, h). At 9 mAh cm^{-2} , a dendrite-
330 free and smooth Li morphology was observed, as seen in Fig. 6i without top plating of Li
331 (Supplementary Fig. 14l). The absence of the top plating for d-CP suggests that the reduced
332 nucleation overpotential (Supplementary Fig. 14a-c) by Li-NW can induce homogenous initial
333 nucleation at the interior of d-CP.

334 The irreversibility of the anode was quantitatively analyzed by investigating single Li
335 plating/stripping cycle after a prior SEI formation and subsequent partial cycling of carbon
336 lithiation/delithiation in a carbonate electrolyte. (Fig. 6j and k). The irreversible capacity of the
337 first cycling originates from the formation of SEI on deposited Li and of isolated Li, whereas
338 that of the second partial cycling should reflect the restoration of the SEI on the current
339 collector damaged during the first cycle. The capacity loss from the first cycle was 0.541 mAh
340 cm^{-2} (CE of 92.4 %) for p-CP (Fig. 6j), which points out that a large amount of Li was lost due

341 to isolated-Li and SEI on metallic Li. The irreversible capacity at the second cycle was 0.143
342 mAh cm⁻², which means the fracture of the pre-formed SEI on p-CP is significant. By contrast,
343 for d-CP, the first cycle irreversible capacity was 0.152 mAh cm⁻² (CE of 97.0 %), which is
344 about one-fourth of that of p-CP (Fig. 6k). Remarkably, the second cycling irreversible capacity
345 due to the restoration of the SEI was nearly zero; this indicates that the SEI on d-CP may not
346 be significantly damaged due to the uniformity of Li plating/stripping and, even if damaged,
347 fractured SEI can be repaired with a minimal amount of electrolyte due to the low Fermi-level
348 of d-CP. In overall, the interfacial instability of p-CP can be attributed to 1) thick and
349 inhomogeneous SEI formation on p-CP, 2) whisker-shaped Li morphology that is prone to Li
350 corrosion by electrolyte, and 3) fracture of the SEI triggering cathodic corrosion of Li, as
351 described in Fig. 6l. By contrast, for d-CP, the lateral Li growth reduces the generation of
352 inactive Li and its insulating surface prevents cathodic Li corrosion, thereby increasing the
353 reversibility of galvanostatic cycling (Fig. 6m).

354

355 **Electrochemical performance of AF-LMB with NW defective surfaces**

356 To evaluate the practical applicability of the NW-enriched carbon current collector for AF-
357 LMBs, we fabricated AF-LMBs by using a high-nickel NCM811 ($\text{LiNi}_{0.8}\text{Co}_{0.1}\text{Mn}_{0.1}\text{O}_2$)
358 cathode with a high areal capacity ($> 4.0 \text{ mAh cm}^{-2}$), employing a flooded electrolyte design
359 (electrolyte to capacity ratio (E/C) of $23.8 \mu\text{l mAh}^{-1}$) or a lean electrolyte design (E/C of $4.0 \mu\text{l}$
360 mAh^{-1}), and various current collectors of Cu, p-CP, and d-CP (Fig. 7a). The voltage profile of
361 AF-LMB incorporating d-CP at the first charging (Fig. 7b) showed a distinctive SEI
362 formation/lithiation step and Li deposition step, as observed for the half cells. Figures 7c and
363 d show the cycling performance of the anode-free cells at practical charging and discharging
364 current density of 2 mA cm^{-2} (0.48 C) under the flooded and lean electrolyte condition,
365 respectively. The AF-LMB cell with the Cu current collector under the flooded condition
366 showed 80% capacity retention only at 10 cycles. A slightly improved cycling stability of 80%
367 capacity retention at 20 cycles with a mitigated capacity fade rate was obtained with p-CP,
368 likely due to reduced effective current density, and confined volume change^{51,52}. With the d-
369 CP current collector, the cycling stability of the AF-LMB was improved to 90% capacity
370 retention at 50 cycles, demonstrating its efficacy in stabilizing the anode-free electrode on a
371 full cell level.

372 Under the lean electrolyte condition (Fig. 7d), the Cu and p-CP cells showed a faster capacity
373 fade and significant capacity fluctuation compared with the flooded condition, because of
374 electrolyte depletion in early cycles. In particular, p-CP exhibited a larger reduction of cycling
375 stability under the lean electrolyte condition because of difficulty in preserving the electrolyte-
376 wetting of the porous 3D current collector with the small amount of electrolyte. In strong
377 contrast, the d-CP cell in the lean electrolyte condition exhibited 90% retention at 50 cycles,
378 which is comparable to that in the flooded electrolyte condition. The differences in cycling
379 behavior and voltage profile between the flooded and lean-electrolyte AF-LMBs are described

380 in more detail in Supplementary Fig. 16. The cell-level energy density of AF-LMBs with
381 different current collector was estimated based on the performance shown in Fig. 7d. The AF-
382 LMB with d-CP can deliver a higher gravimetric energy density of 357.7 Wh kg^{-1} together with
383 while 12 times longer cycle life compared with that with Cu (345.4 Wh kg^{-1}) (Supplementary
384 Table 3, Supplementary Fig. 17).

385 The recently reported high cycling stabilities for AF-LMBs were obtained at enhanced
386 temperature or pressure. The cycling stabilities and densely-packed Li deposits presented here
387 have not been achieved at ambient temperature and unpressurized Li deposition^{2,53-62}. It should
388 be stressed that the cycle performance of d-CP in the AF-LMB is not derived from the pressure
389 effect because stack pressure is not delivered to the inner surface of the 3D current collector.
390 As displayed in Fig. 7e, the operation current density and the areal capacity of the AF-LMB
391 with d-CP were higher than the previously reported values obtained with or without external
392 pressurization, emphasizing the advantage of the NW structure. Since control of temperature
393 and pressure in a battery system impose difficulties in battery design for higher energy density,
394 the high cycling stabilities presented here are of high practical importance.

395

396 **Conclusions**

397 We demonstrated dual functionality of an electron-deficient NW defect by experimental and
398 computational analyses. Compared with a graphene surface, the NW defect has a different
399 electronic structure of a low Fermi level due to its electron deficiency. On the NW defect-
400 enriched surface, a thin and defect-free SEI layer was formed and electrolyte decomposition
401 was alleviated. The uniform SEI structure and strong Li-C orbital hybridization promoted
402 uniform Li nucleation and lateral growth, resulting in a densely-packed Li morphology. The
403 NW defect-enriched 3D carbon current collector achieved high reversibility of Li
404 plating/stripping at 5 mAh cm^{-2} and 2 mA cm^{-2} even with a corrosive carbonate electrolyte. It
405 significantly improved the cycling stability of an AF-LMB with high areal capacity (4.2 mAh
406 cm^{-2}) under a lean electrolyte condition (E/C of $4.0 \text{ } \mu\text{l mAh}^{-1}$) without any external
407 pressurization or elevated temperature. Based on the model system provided herein regarding
408 how the electronic structure of the current collector controls the SEI microstructure and Li
409 nucleation, a rational design strategy for advancing AF-LMBs is presented.

410 **Methods**

411 **Synthesis of the defective carbon layer-coated carbon paper electrode.** A highly defective carbon layer-
412 coated 3D current collector was synthesized by a well-established solution-synthesis method^{63,64}. The surface of
413 a carbon fiber paper (HCP010N, Shanghai Hesen Electric Co. Ltd. USA) was oxidized by oxygen plasma
414 treatment. Zinc nitrate hexahydrate (5.95 g, 1 eq.) and 2-methyl imidazole (13.16 g, 8 eq.) were separately
415 dissolved in 100 ml of methanol. The surface-oxidized CP was immersed in a mixture of solutions of Zn^{2+} (15 ml)
416 and 2-methyl imidazole (15 ml) for 12 h, to coat ZIF-8 on its surface. The samples were then thoroughly washed
417 with ethanol many times to remove any remaining solvents. The ZIF-8 coating procedure was repeated two times.
418 The ZIF-8@CP was dried under a vacuum overnight. Then, to form d-CP, it was carbonized with heating at a
419 temperature ramp rate of $5\text{ }^{\circ}\text{C min}^{-1}$ to $1000\text{ }^{\circ}\text{C}$ under a N_2 atmosphere and holding for 5 h. The carbonized d-CP
420 was immersed in 2 M hydrochloric acid with stirring at room temperature for 6 h, followed by rinsing with distilled
421 deionized water (DI) several times and drying under a vacuum at 70°C for 7 h.

422

423 **Electrochemical test.** Electrochemical half-cell tests for the current collectors were conducted with a CR2032-
424 type coin-cell using Li foil (450 μm thickness, Honjo Metal) as a counter electrode, a Celgard 2400 PP separator,
425 and 1 M LiPF_6 EC/DEC(1/1) +10% FEC+1% VC electrolyte (100 μl). After a pre-cycle at 0.2 mA cm^{-2} between
426 2.0 and 0 V, galvanostatic cycling was conducted at 5 mAh cm^{-2} and 2 mA cm^{-2} with a stripping potential cut-off
427 of 1.0 V. The symmetric cell was assembled with two pieces of Li-plated copper or carbon current collectors. The
428 Li plating on the current collectors was conducted with 1M LiTFSI DOL/DME (1/1 in volume) + 1% LiNO_3
429 electrolyte at 0.1 mA cm^{-2} . After the electroplating process, the Li-plated electrode was rinsed with DME. With
430 the two pre-lithiated anodes and 100 μl of 1M LiTFSI DOL/DME v/v 1:1 1% LiNO_3 electrolyte, symmetric cells
431 were assembled. An anode-free cell test was conducted with a 2032 coin-type cell using a $\text{LiNi}_{0.8}\text{Mn}_{0.1}\text{Co}_{0.1}\text{O}_2$
432 (NCM811) cathode (4.2 mAh cm^{-2}), a current collector (Cu, p-CP, d-CP), a Celgard 2400 PP separator, and 1 M
433 LiPF_6 EC/DEC+10% FEC+1% VC electrolyte in a voltage range of 2.7 V to 4.3 V at 0.48/0.48 C
434 (charge/discharge). After the constant current charging step, constant voltage at 4.3 V was set for potentiostatic
435 charging until the current density reaches 0.02 C. Two pre-cycles were conducted at 0.1/0.1 C (charge/discharge).
436 All the cell assembly processes were conducted in an Ar-filled glovebox. A WBCS3000L battery tester was used
437 for the cell tests.

438

439 **Structural characterizations.** A SEM analysis was performed using a Field-Emission Scanning Electron
440 Microscope (FE-SEM, Sirion by FEI) with 10 kV accelerating voltage and 5.0 mm working distance (Z-height).
441 TEM and TEM-EDX analyses were carried out using a Transmission Electron Microscope (TEM, Tecnai G2 F30)
442 with 200 kV accelerating voltage. The SEI formed on current collectors was ground and dispersed in DEC. The
443 upper solution was sampled with a micropipette and loaded onto the TEM grid. The Raman spectra were measured
444 using a Raman spectroscopy (HORIBA Jobin Yvon, France) with a confocal microscope equipped with a solid-
445 state crystal laser (the wave length of 514.5 nm and excitation energy of 2.41 eV) and a spot size of 0.5 mm. N₂
446 adsorption and desorption isotherms were obtained at 87 K on a Micromeritics 3Flex Surface Characterization
447 Analyzer. UPS analysis of the electrode work function with potential variation was conducted using In-Situ X-
448 ray Photoelectron Spectroscopy (Axis-Supra by Kratos) with a He I X-ray source (hν=21.2 eV). The samples for
449 the UPS analysis were prepared by galvanostatic lithiation at 50 μA cm⁻² with various cut-off voltages (2.0 V, 1.5
450 V, and 1.0 V vs. Li/Li⁺ in 1 M LiPF₆ EC/DEC), rinsed with dimethyl carbonate (DEC), and dried at 60 °C
451 overnight before the measurement. To obtain the secondary cut-off region, 9.0 V bias was applied to the samples.
452 The Fermi level of the samples were aligned with gold (Au) reference metal. For the work function calculation,
453 the UPS data of the low kinetic energy cut-off region (secondary cut-off region) were extrapolated, and intercept
454 points with the baseline were subtracted from the incident photon energy ($\Phi_{\text{electrode}}=21.2 \text{ eV} - (\text{binding energy of}$
455 $\text{intercept point})$). SEI composition and defective structure of the electrodes were analyzed by X-ray Photoelectron
456 Spectroscopy (XPS, K-alpha by Thermo VG Scientific) with an Al X-ray source (hν=1486.7 eV). The binding
457 energies obtained from the XPS analysis were calibrated with the C-C bond peak of 284.8 eV at C1s spectra. An
458 operando-XRD analysis was performed using an in-situ Battery Cell X-ray Diffractometer (in-situ XRD, R-Axis
459 IV by RIGAKU) with a transmission Cu Kα X-ray source. The test cell had a 1.5 mm hole, which was sealed by
460 a transparent mylar film and epoxy 4460.

461

462 **References**

- 463 1 Zhang, J.-G. Anode-less. *Nat. Energy* **4**, 637-638 (2019).
- 464 2 Weber, R. *et al.* Long cycle life and dendrite-free lithium morphology in anode-free lithium pouch cells
465 enabled by a dual-salt liquid electrolyte. *Nat. Energy* **4**, 683-689 (2019).
- 466 3 Beyene, T. T. *et al.* Concentrated dual-salt electrolyte to stabilize Li metal and increase cycle life of
467 anode free Li-metal batteries. *J. Electrochem. Soc.* **166**, A1501-A1509 (2019).
- 468 4 Qian, J. *et al.* Anode-free rechargeable lithium metal batteries. *Adv. Funct. Mater.* **26**, 7094-7102 (2016).
- 469 5 Lin, D. *et al.* Fast galvanic lithium corrosion involving a Kirkendall-type mechanism. *Nat. Chem.* **11**,
470 382-389 (2019).
- 471 6 Liu, J. *et al.* Pathways for practical high-energy long-cycling lithium metal batteries. *Nat. Energy* **4**, 180-
472 186 (2019).
- 473 7 Yan, K. *et al.* Selective deposition and stable encapsulation of lithium through heterogeneous seeded
474 growth. *Nat. Energy* **1**, 1-8 (2016).
- 475 8 Niu, C. *et al.* Self-smoothing anode for achieving high-energy lithium metal batteries under realistic
476 conditions. *Nat. Nanotechnol.* **14**, 594-601 (2019).
- 477 9 Chen, Y. *et al.* Li metal deposition and stripping in a solid-state battery via Coble creep. *Nature*, 1-5
478 (2020).
- 479 10 Chen, X. *et al.* Lithiophilicity chemistry of heteroatom-doped carbon to guide uniform lithium nucleation
480 in lithium metal anodes. *Sci. Adv.* **5**, eaau7728 (2019).
- 481 11 Lu, Z. *et al.* Graphitic carbon nitride induced micro-electric field for dendrite-free lithium metal anodes.
482 *Adv. Energy Mater.* **9**, 1803186 (2019).
- 483 12 Xie, J. *et al.* Engineering stable interfaces for three-dimensional lithium metal anodes. *Sci. Adv.* **4**,
484 eaat5168 (2018).
- 485 13 Zheng, J. *et al.* Reversible epitaxial electrodeposition of metals in battery anodes. *Science* **366**, 645-648
486 (2019).
- 487 14 Genovese, M. *et al.* Hot formation for improved low temperature cycling of anode-free lithium metal
488 batteries. *J. Electrochem. Soc.* **166**, A3342-A3347 (2019).
- 489 15 Beyene, T. T. *et al.* Effects of concentrated salt and resting protocol on solid electrolyte interface
490 formation for improved cycle stability of anode-free lithium metal batteries. *ACS Appl. Mater. Interfaces*
491 **11**, 31962-31971 (2019).

492 16 Pei, A., Zheng, G., Shi, F., Li, Y. & Cui, Y., Nanoscale nucleation and growth of electrodeposited
493 lithium metal. *Nano Lett.* **17**, 1132-1139 (2017).

494 17 Yan, K. *et al.* Temperature-dependent nucleation and growth of dendrite-free lithium metal anodes.
495 *Angew. Chem. Int. Ed.* **131**, 11486-11490 (2019).

496 18 Wang, J. *et al.* Improving cyclability of Li metal batteries at elevated temperatures and its origin revealed
497 by cryo-electron microscopy. *Nat. Energy* **4**, 664-670 (2019).

498 19 Hao, F., Verma, A. & Mukherjee, P. P. Mechanistic insight into dendrite–SEI interactions for lithium
499 metal electrodes. *J. Mater. Chem. A* **6**, 19664-19671 (2018).

500 20 Wang, A., Kadam, S., Li, H., Shi, S. & Qi, Y. Review on modeling of the anode solid electrolyte
501 interphase (SEI) for lithium-ion batteries. *Npj Comput. Mater* **4**, 15 (2018).

502 21 Schejn, A. M. *Synthesis and catalytic activity of ZIF-8 and doped-ZIF-8 crystals: stability and*
503 *cytotoxicity evaluation*, (Doctoral dissertation, University of Lorraine, 2015).

504 22 Zhang, L. *et al.* Highly graphitized nitrogen-doped porous carbon nanopolyhedra derived from ZIF-8
505 nanocrystals as efficient electrocatalysts for oxygen reduction reactions. *Nanoscale* **6**, 6590-6602 (2014).

506 23 Fu, F. *et al.* Size-controllable synthesis of zeolitic imidazolate framework/carbon nanotube composites.
507 *Crystals* **8**, 367 (2018).

508 24 Gadipelli, S. & Guo, Z. X. J. C. Tuning of ZIF-derived carbon with high activity, nitrogen functionality,
509 and yield—a case for superior CO₂ capture. *ChemSusChem* **8**, 2123-2132 (2015).

510 25 Bonaccorso, F. *et al.* Production and processing of graphene and 2d crystals. *Mater. Today* **15**, 564-589
511 (2012).

512 26 Ganesan, K. *et al.* A comparative study on defect estimation using XPS and Raman spectroscopy in few
513 layer nanographitic structures. *Phys. Chem. Chem. Phys.* **18**, 22160-22167 (2016).

514 27 Barinov, A. *et al.* Initial stages of oxidation on graphitic surfaces: photoemission study and density
515 functional theory calculations. *J. Phys. Chem. C* **113**, 9009-9013 (2009).

516 28 Kim, W., Lee, T. & Han, S. Multi-layer graphene/copper composites: Preparation using high-ratio
517 differential speed rolling, microstructure and mechanical properties. *Carbon* **69**, 55-65 (2014).

518 29 Ferrari, A. C. *et al.* Raman spectrum of graphene and graphene layers. *Phys. Rev. Lett.* **97**, 187401 (2006).

519 30 Ji, K. *et al.* Lithium intercalation into bilayer graphene. *Nat. Commun.* **10**, 275 (2019).

520 31 Lin, Y.-X. *et al.* Connecting the irreversible capacity loss in Li-ion batteries with the electronic insulating
521 properties of solid electrolyte interphase (SEI) components. *J. Power Sources* **309**, 221-230 (2016).

522 32 Li, H. *et al.* Revealing principles for design of lean-electrolyte lithium metal anode via in situ
523 spectroscopy. *J. Am. Chem. Soc.* **142**, 2012-2022 (2020).

524 33 Gialampouki, M. A., Hashemi, J. & Peterson, A. A. J. T. J. o. P. C. C. The electrochemical mechanisms
525 of solid–electrolyte interphase formation in lithium-based batteries. *J. Phys. Chem. C* **123**, 20084-20092
526 (2019).

527 34 Jain, S. & Krishnan, K. S. The thermionic constants of metals and semi-conductors I. Graphite. *Proc.*
528 *Math. Phys. Eng. Sci.* **213**, 143-157 (1952).

529 35 Legrain, F. *et al.* Amorphous (glassy) carbon, a promising material for sodium ion battery anodes: a
530 combined first-principles and experimental study. *J. Phys. Chem. C* **119**, 13496-13501 (2015).

531 36 Mukherjee, R. *et al.* Defect-induced plating of lithium metal within porous graphene networks. *Nat.*
532 *Commun.* **5**, 3710 (2014).

533 37 Asenbauer, J. *et al.* The success story of graphite as a lithium-ion anode material–fundamentals,
534 remaining challenges, and recent developments including silicon (oxide) composites. *Sustain. Energy*
535 *Fuels* **4**, 5387-5416 (2020).

536 38 Hess, M. *Kinetics and stage transitions of graphite for lithium-ion batteries* (ETH Zurich, Zürich, 2013).

537 39 Zhou, L.-J., Hou, Z. F. & Wu, L.-M. First-Principles Study of Lithium Adsorption and Diffusion on
538 Graphene with Point Defects. *J. Phys. Chem. C* **116**, 21780-21787 (2012).

539 40 Li, T., Tang, X., Liu, Z. & Zhang, P. Effect of intrinsic defects on electronic structure of bilayer graphene:
540 First-principles calculations. *Physica E Low Dimens. Syst. Nanostruct.* **43**, 1597-1601 (2011).

541 41 Denis, P. A., Faccio, R. & Iribarne, F. How is the stacking interaction of bilayer graphene affected by
542 the presence of defects? *Comput. Theor. Chem.* **995**, 1-7 (2012).

543 42 Meng, Q. *et al.* Heterogeneous nucleation and growth of electrodeposited lithium metal on the basal
544 plane of single-layer graphene. *Energy Storage Mater.* **16**, 419-425 (2019).

545 43 Steiger, J. *Mechanisms of dendrite growth in lithium metal batteries*. (Doctoral dissertation, Karlsruhe
546 Institute of Technology, 2015).

547 44 Hepel, T. Effect of surface diffusion in electrodeposition of fractal structures. *J. Electrochem. Soc.* **134**,
548 2685 (1987).

549 45 Zhu, M. *et al.* Homogeneous guiding deposition of sodium through main group II metals toward dendrite-
550 free sodium anodes. *Sci. Adv.* **5**, eaau6264 (2019).

551 46 Mamme, M. H., Köhn, C., Deconinck, J. & Ustarroz, J. J. N. Numerical insights into the early stages of
552 nanoscale electrodeposition: nanocluster surface diffusion and aggregative growth. *Nanoscale* **10**, 7194-
553 7209 (2018).

554 47 Budevski, E. B., Staikov, G. T. & Lorenz, W. J. *Electrochemical phase formation and growth: an*
555 *introduction to the initial stages of metal deposition*. (VCH, Weinheim, 1996).

556 48 Vilá, R. A., Huang, W. & Cui, Y. Nickel impurities in the solid-electrolyte interphase of lithium-metal
557 anodes revealed by cryogenic electron microscopy. *Cell Rep. Phys. Sci.*, 100188 (2020).

558 49 Ju, Z. *et al.* Biomacromolecules enabled dendrite-free lithium metal battery and its origin revealed by
559 cryo-electron microscopy. *Nat. Commun.* **11**, 488 (2020).

560 50 Li, Y. *et al.* Atomic structure of sensitive battery materials and interfaces revealed by cryo-electron
561 microscopy. *Science* **358**, 506-510 (2017).

562 51 Zuo, T. T. *et al.* Graphitized carbon fibers as multifunctional 3D current collectors for high areal capacity
563 Li anodes. *Adv. Mater.* **29**, 1700389 (2017).

564 52 Shi, P. *et al.* Lithiophilic LiC₆ layers on carbon hosts enabling stable Li metal anode in working batteries.
565 *Adv. Mater. Interfaces* **31**, 1807131 (2019).

566 53 Yu, Z. *et al.* Molecular design for electrolyte solvents enabling energy-dense and long-cycling lithium
567 metal batteries. *Nat. Energy* **5**, 526-533 (2020).

568 54 Qiu, F. *et al.* A concentrated ternary-salts electrolyte for high reversible Li metal battery with slight
569 excess Li. *Adv. Energy Mater.* **9**, 1803372 (2019).

570 55 Fan, X. *et al.* Non-flammable electrolyte enables Li-metal batteries with aggressive cathode chemistries.
571 *Nat. Nanotechnol.* **13**, 715-722 (2018).

572 56 Suo, L. *et al.* Fluorine-donating electrolytes enable highly reversible 5-V-class Li metal batteries. *PNAS*
573 **115**, 1156-1161 (2018).

574 57 Hagos, T. T. *et al.* Locally concentrated LiPF₆ in a carbonate-based electrolyte with fluoroethylene
575 carbonate as a diluent for anode-free lithium metal batteries. *ACS Appl. Mater. Interfaces* **11**, 9955-9963
576 (2019).

577 58 Zhang, S. S., Fan, X. & Wang, C. A tin-plated copper substrate for efficient cycling of lithium metal in
578 an anode-free rechargeable lithium battery. *Electrochim. Acta* **258**, 1201-1207 (2017).

579 59 Wondimkun, Z. T. *et al.* Binder-free ultra-thin graphene oxide as an artificial solid electrolyte interphase
580 for anode-free rechargeable lithium metal batteries. *J. Power Sources* **450**, 227589 (2020).

581 60 Chen, W. *et al.* Laser-induced silicon oxide for anode-free lithium metal batteries. *Adv. Mater.* **32**,
582 2002850 (2020).

583 61 Assegie, A. A., Cheng, J.-H., Kuo, L.-M., Su, W.-N. & Hwang, B.-J. Polyethylene oxide film coating
584 enhances lithium cycling efficiency of an anode-free lithium-metal battery. *Nanoscale* **10**, 6125-6138
585 (2018).

586 62 Assegie, A. A. *et al.* Multilayer-graphene-stabilized lithium deposition for anode-free lithium-metal
587 batteries. *Nanoscale* **11**, 2710-2720 (2019).

588 63 Park, M.-J. & Lee, J.-S. Zeolitic-imidazole framework thin film-based flexible resistive switching
589 memory. *RSC Adv.* **7**, 21045-21049 (2017).

590 64 Xu, X. *et al.* The surface coating of commercial LiFePO₄ by utilizing ZIF-8 for high electrochemical
591 performance lithium ion battery. *Nano-Micro Lett.* **10**, 1 (2018).

592

593 **Competing interests**

594 The authors declare no competing interests.

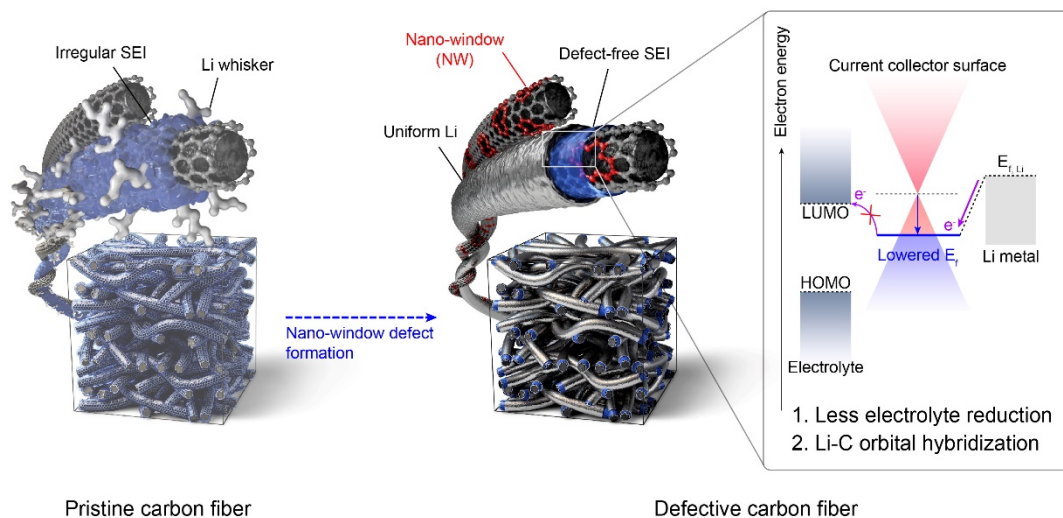
595

596 **Supplementary information**

597 Supplementary Information

598 Supplementary Figs. 1–17

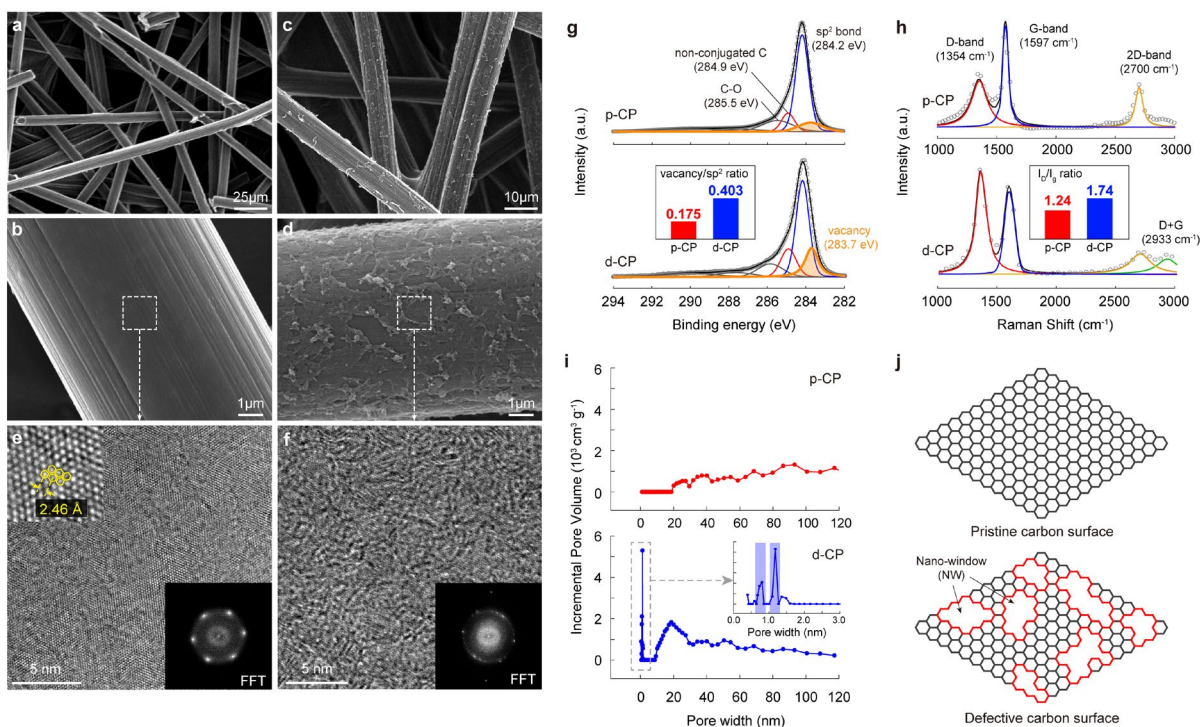
599 Supplementary Tables 1-3



600

601 **Fig. 1 | Schematic of the dual functionality of electron-deficient defective carbon surface.**

602 Pristine 3D-carbon fiber electrode with graphitic surface (p-CP) forming a non-uniform SEI (blue layer) and
 603 dendritic Li deposit (silver color protrusion), and defective carbon layer-decorated carbon fiber electrode (d-CP)
 604 inducing defect-free SEI and dendrite-free Li morphology. Suppression of electron tunneling to the electrolyte at
 605 the defective carbon surface of d-CP via a lower Fermi-level (larger work function) in contrast to the graphitic
 606 carbon surface of p-CP. Orbital hybridization between lithium deposit and carbon defect on the defective carbon
 607 surface of d-CP due to its low Fermi-level.



608

609 **Fig. 2: Atomistic structure of the defective carbon layer. a-d,** SEM images of p-CP (a, b) and d-

610 CP (c, d). **e,f,** HR-TEM images and corresponding FFT patterns for p-CP (e) and d-CP (f). **g,** C1s HR-XRS spectra

611 for p-CP and d-CP. The binding energy in XPS was calibrated with the C1s sp² peak as 284.2 eV. (Inset:

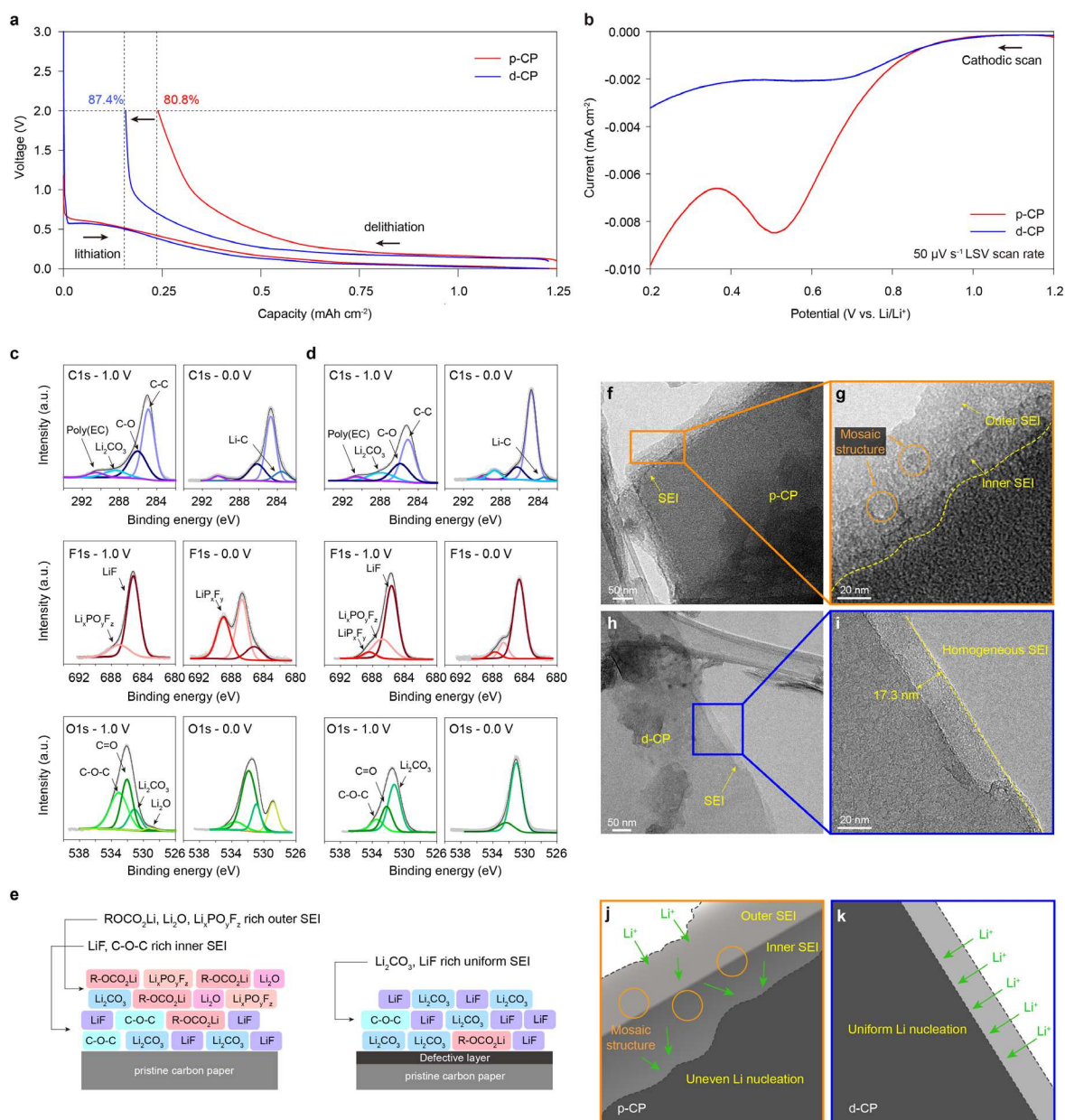
612 Comparison of the vacancy/sp² ratio determined by dividing the area of the vacancy peak by that of the sp² peak

613 between p-CP and d-CP) **h,** Raman spectra for p-CP and d-CP. (Inset: Comparison of I_D/I_G ratio calculated by

614 dividing the area of the D-band by that of the G-band between p-CP and d-CP) **i,** BJH pore size distribution

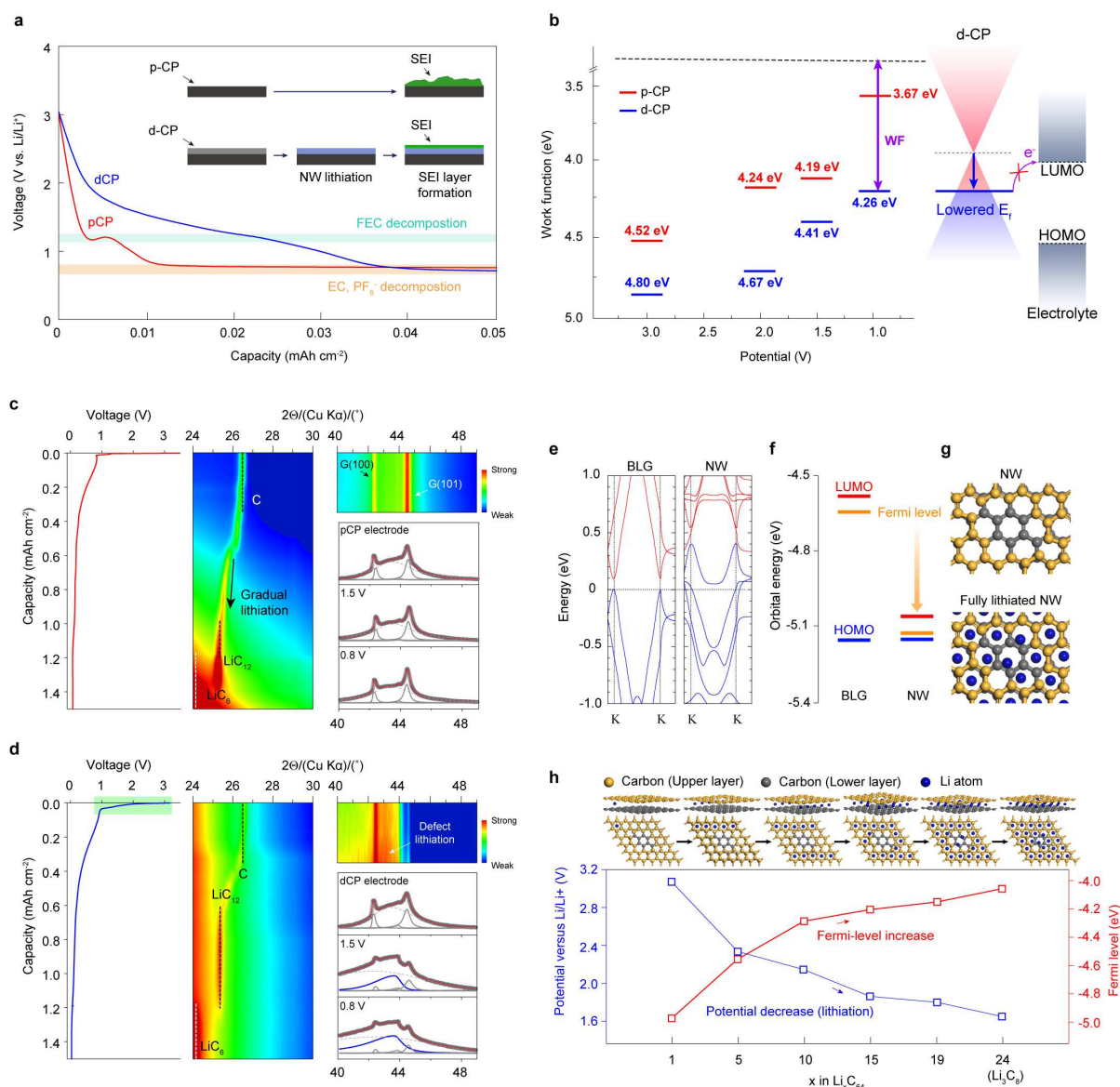
615 analysis for p-CP and d-CP. Inset is the magnified micropore region for d-CP. **j,** Schematic illustrations of the

616 atomistic structure of p-CP and d-CP surface. The red line indicates the NW structure of d-CP.



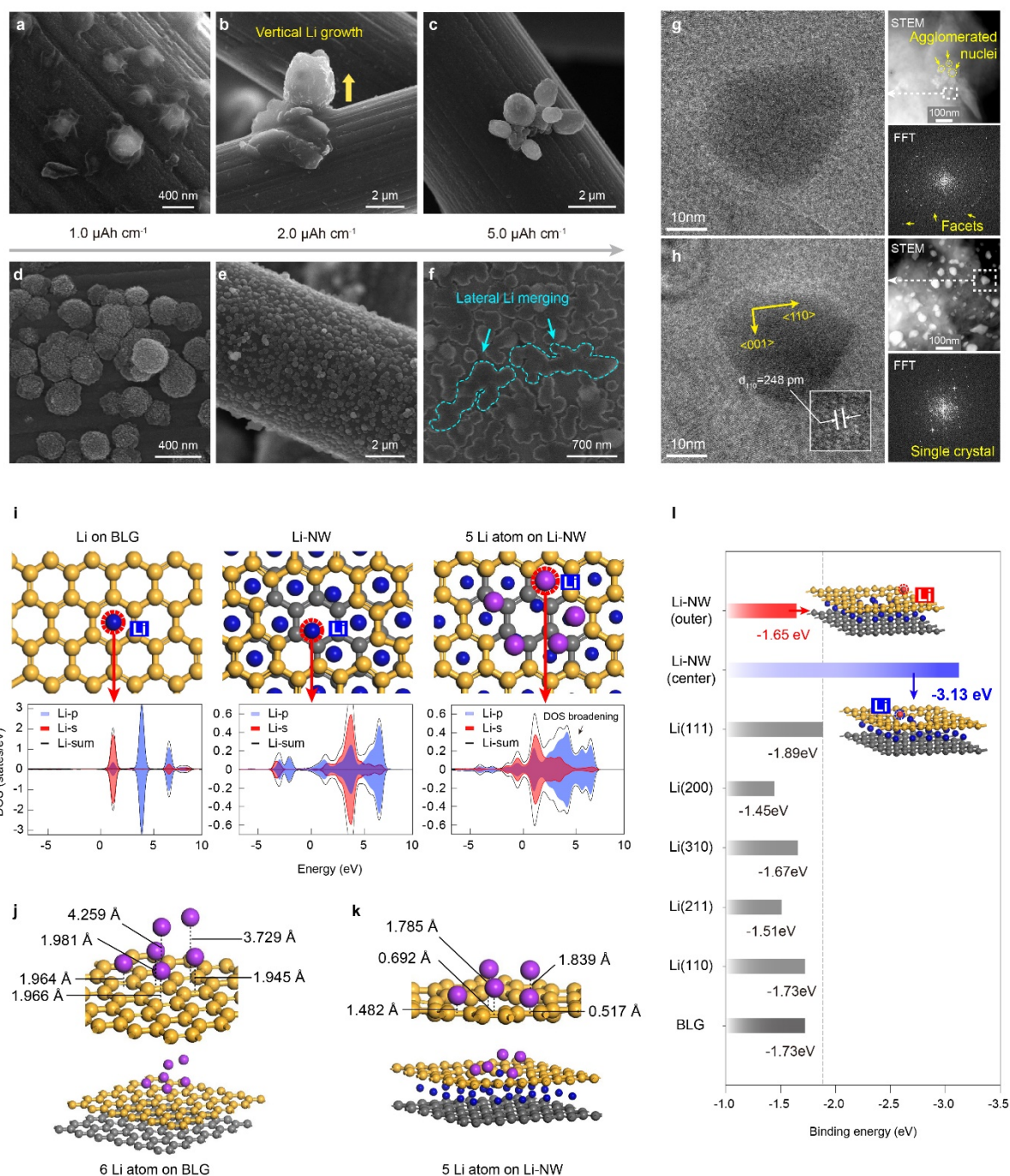
617

618 **Fig. 3: Thin and defect-free SEI formation on the defective layer.** **a**, Galvanostatic lithiation-
 619 delithiation curves for Li||p-CP and Li||d-CP cell in the range of 0.0 to 2.0 V at 0.1 mA cm⁻² for quantification of
 620 irreversible capacity at the first cycle due to the electrolyte decomposition at the current collector. **b**, Current
 621 density from electrolyte decomposition based on the active surface area of the current collector (Supplementary
 622 Figs. 2a, b) during the LSV measurement (cathodic scan) at 50 μV s⁻¹ scan rate for Li||p-CP and Li||d-CP half-
 623 cells. **c, d**, Ex-situ XPS analysis for the SEI layer on p-CP (**c**) and d-CP (**d**). The left spectra were taken after
 624 galvanostatic reduction at 0.1 mA cm⁻² down to 1.0 V (inner SEI), and the right spectra to 0.0 V (outer SEI). The
 625 binding energy was calibrated with the C-C bond peak of 285 eV in C1s spectra. **e**, Suggested SEI composition
 626 on p-CP (left) and d-CP (right). **f-i**, TEM images of the SEI layers for p-CP (**f, g**) and d-CP (**h, i**) after the
 627 galvanostatic reduction to 0.0 V **j, k**, Schematic representation of the microstructure of SEI formed on p-CP (**j**)
 628 and d-CP (**k**).



629

630 **Fig. 4: Lithiation of NW structure and electronic property of defect.** **a**, Voltage profile for the
 631 early stage of galvanostatic lithiation for p-CP and d-CP at 0.1 mA cm^{-2} in half-cell configuration . **b**, Plots of
 632 work function for p-CP and d-CP as a function of electrode potential from OCV to 1.0 V (V vs. Li/Li^+) determined
 633 from extrapolation of the secondary cut-off region in UPS (Supplementary Fig. 3). **c**, **d**, Image plots of operando
 634 XRD spectra along with the potential profile during the first lithiation and deconvoluted XRD patterns at OCV,
 635 1.5 V and 0.8 V for p-CP (c) and d-CP (d). The peaks from the lithiated defect structure (lithiated NW, Li_3C_8) at
 636 43° of 2θ are indicated by blue lines. **e**, Band structures for perfect BLG and NW defect. The Fermi-level was set
 637 to zero. **f**, Comparison of HOMO, LUMO, and Fermi-level for BLG and NW. **g**, The relaxed structures of NW
 638 and fully lithiated NW (Li_3C_8). The structure of lithiated NW was constructed according to the voltage profiles
 639 and XRD spectra. **h**, DFT calculations of Fermi-level and redox potential for NW at various lithiation degrees.
 640 The Li, carbon at the upper layer, and carbon at the lower layer are shown in blue, yellow, and gray color,
 641 respectively.



642

643 **Fig. 5: Mechanistic analysis for morphological propensity of Li nucleation and growth on**

644 **NW structure a-f**, SEM images of the Li deposit morphology on p-CP (a-c) and d-CP (d-f) after Li deposition

645 at 1.0 mA cm⁻² for 3.6, 7.2, and 18 s, which correspond to 1, 2, and 5 μAh cm⁻², respectively. **g, h**, TEM, STEM,

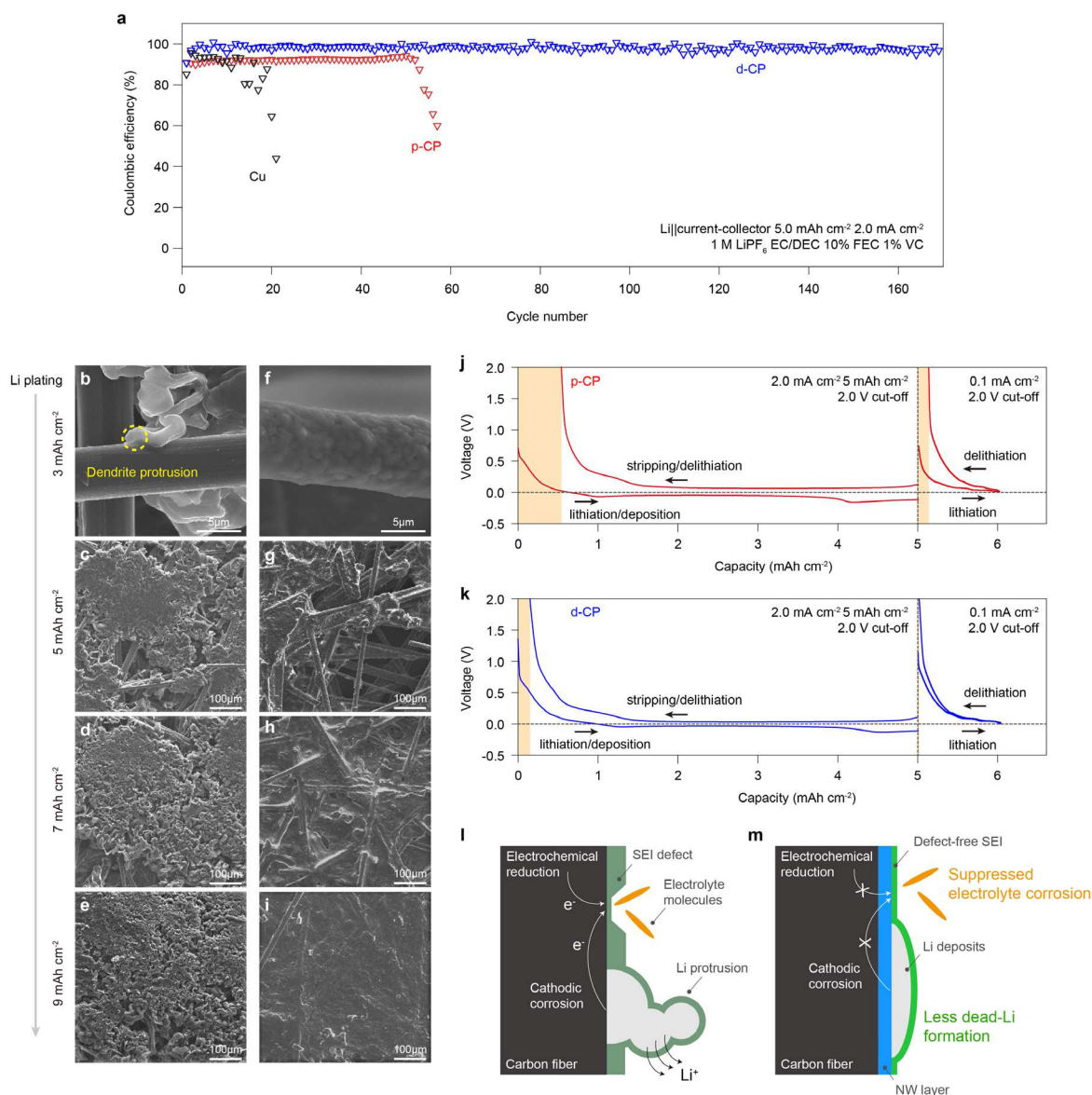
646 and FFT images of Li nuclei on p-CP (g) and d-CP (h) at 1.0 mA cm⁻², 1 μAh cm⁻². **i**, Relaxed structures and

647 pDOSs of single Li atom adsorbed on perfect BLG, Li-NW, and Li-NW with four pre-adsorbed Li atoms. **j, k**,

648 Relaxed configurations of Li atom cluster adsorbed on perfect BLG and Li-NW (Li₃C₈). The lithiated Li, Li cluster,

649 carbon at the upper layer, and carbon at the lower layer are shown in blue, purple, yellow, and gray color,

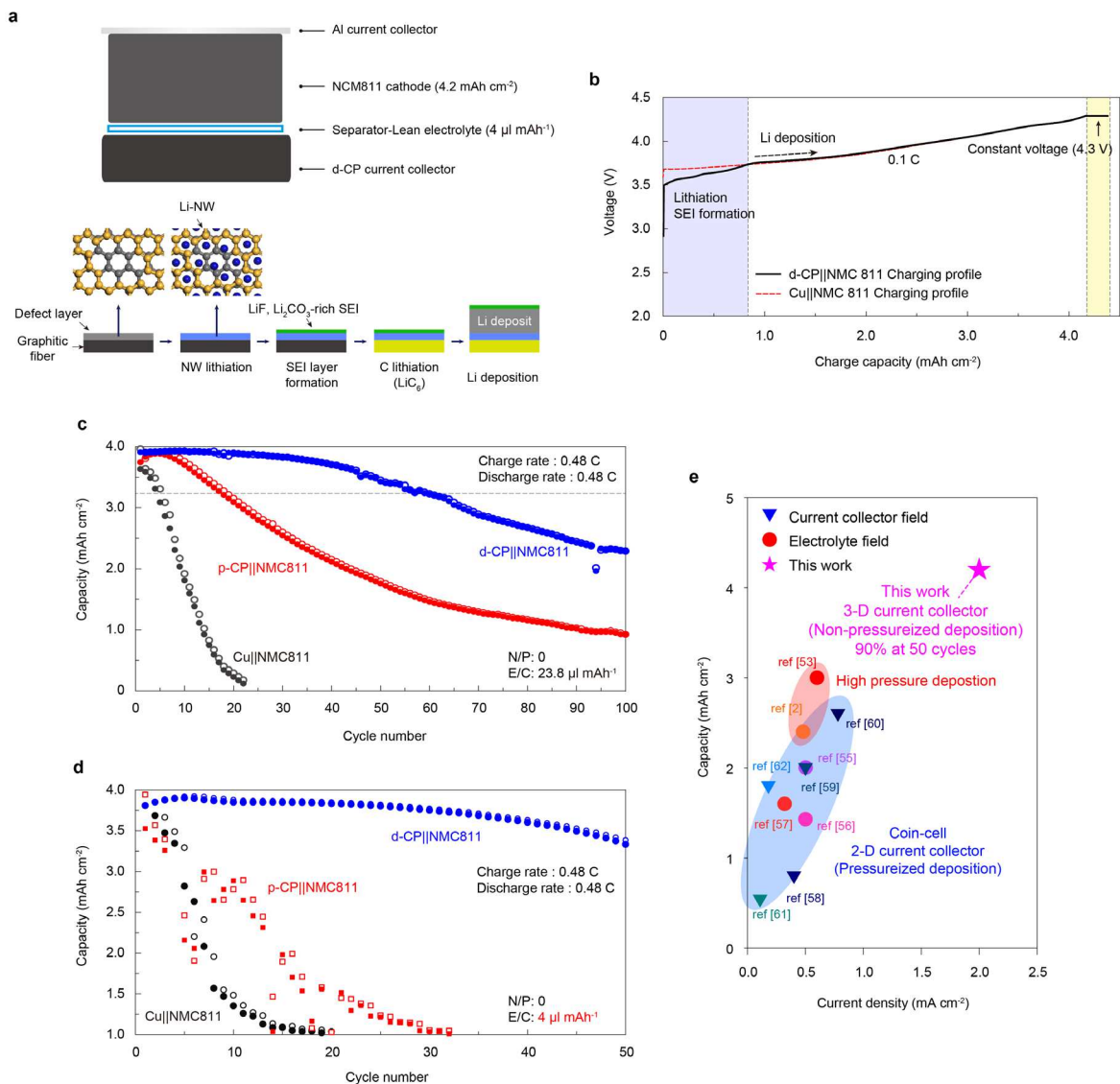
650 respectively. **1**, Binding energies of Li atom on the outer and center of Li-NW, various facets ((111), (200), (310),
651 (211), (110)) of Li metal, and perfect BLG.



652

653 **Fig 6: Reversibility of Li plating/stripping on the defective carbon surface.** **a**, The plots of CE
 654 as a function of cycle number for Cu, p-CP, and d-CP current collector in half-cell configuration at a current
 655 density of 2.0 mA cm⁻² and a capacity of 5.0 mAh cm⁻². **b-i**, Li deposition morphologies for p-CP (b-e) and d-CP
 656 (f-i) at various plating capacities from 3.0 to 9.0 mAh cm⁻². **j, k**, Quantification of irreversible capacity derived
 657 by Li metal plating/stripping and sequential restoration of damaged SEI on current collector surface. The
 658 restoration of SEI was performed by galvanostatic cycling with voltage cut-off of 0 V to 2.0 V at a current density
 659 of 0.1 mA cm⁻². **l, m**, Schematics for the irreversible loss of Li and the electrolyte on p-CP surface (l), and the
 660 proposed mechanism for prevention of the irreversibility on d-CP surface (m).

661



662

663 **Fig 7: Electrochemical performance of AF-LMB with d-CP under realistic conditions. a,**

664 Configuration of anode-free cells with d-CP and high loading (4.2 mAh cm^{-2}) NCM811 cathode; evolution of the

665 anode structure during the first charging. **b,** Voltage profiles of the AF- NCM811 full cell with Cu or d-CP during

666 the charging at 0.1 C and sequential constant voltage charging at 4.3 V (cut-off current: 0.02 C). **c, d,** The plots

667 of discharge (filled symbols) and charge (open symbols) capacities as a function of cycle number for the AF-

668 NCM811 full cells with 1M LiPF_6 EC/DEC 10% FEC 1% VC in a flooded cell condition (c) (E/C ratio of $23.8 \mu\text{l mAh}^{-1}$) and a lean electrolyte condition (d) (E/C ratio of $4.0 \mu\text{l mAh}^{-1}$). The flooded and lean electrolyte cells

669 were cycled at a charge/discharge rate of 0.48 C (2 mA cm^{-2}) with a potential window of 2.7-4.3 V. **e,** Comparison

670 of the areal capacity and current density ensuring stable operation for this work and previous works.

671

672

Figures

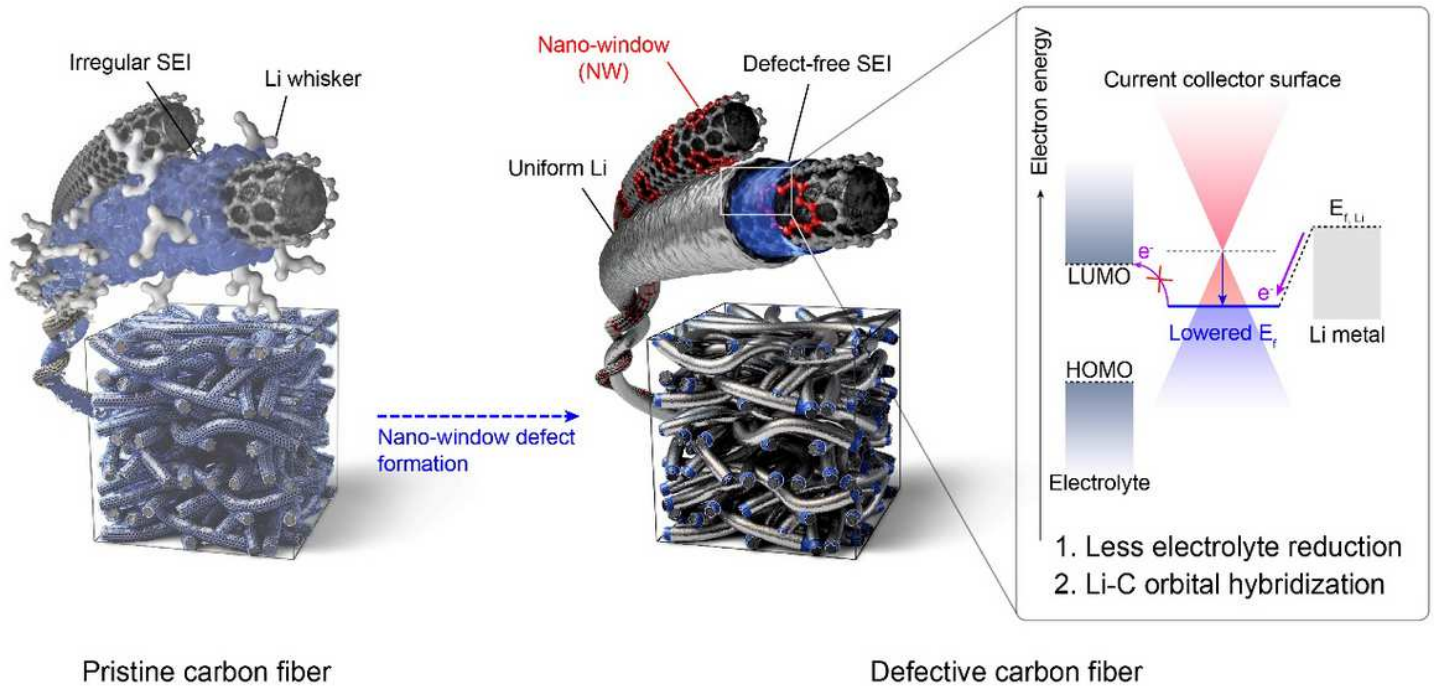


Figure 1

Schematic of the dual functionality of electron-deficient defective carbon surface. Pristine 3D-carbon fiber electrode with graphitic surface (p-CP) forming a non-uniform SEI (blue layer) and dendritic Li deposit (silver color protrusion), and defective carbon layer-decorated carbon fiber electrode (d-CP) inducing defect-free SEI and dendrite-free Li morphology. Suppression of electron tunneling to the electrolyte at the defective carbon surface of d-CP via a lower Fermi-level (larger work function) in contrast to the graphitic carbon surface of p-CP. Orbital hybridization between lithium deposit and carbon defect on the defective carbon surface of d-CP due to its low Fermi-level.

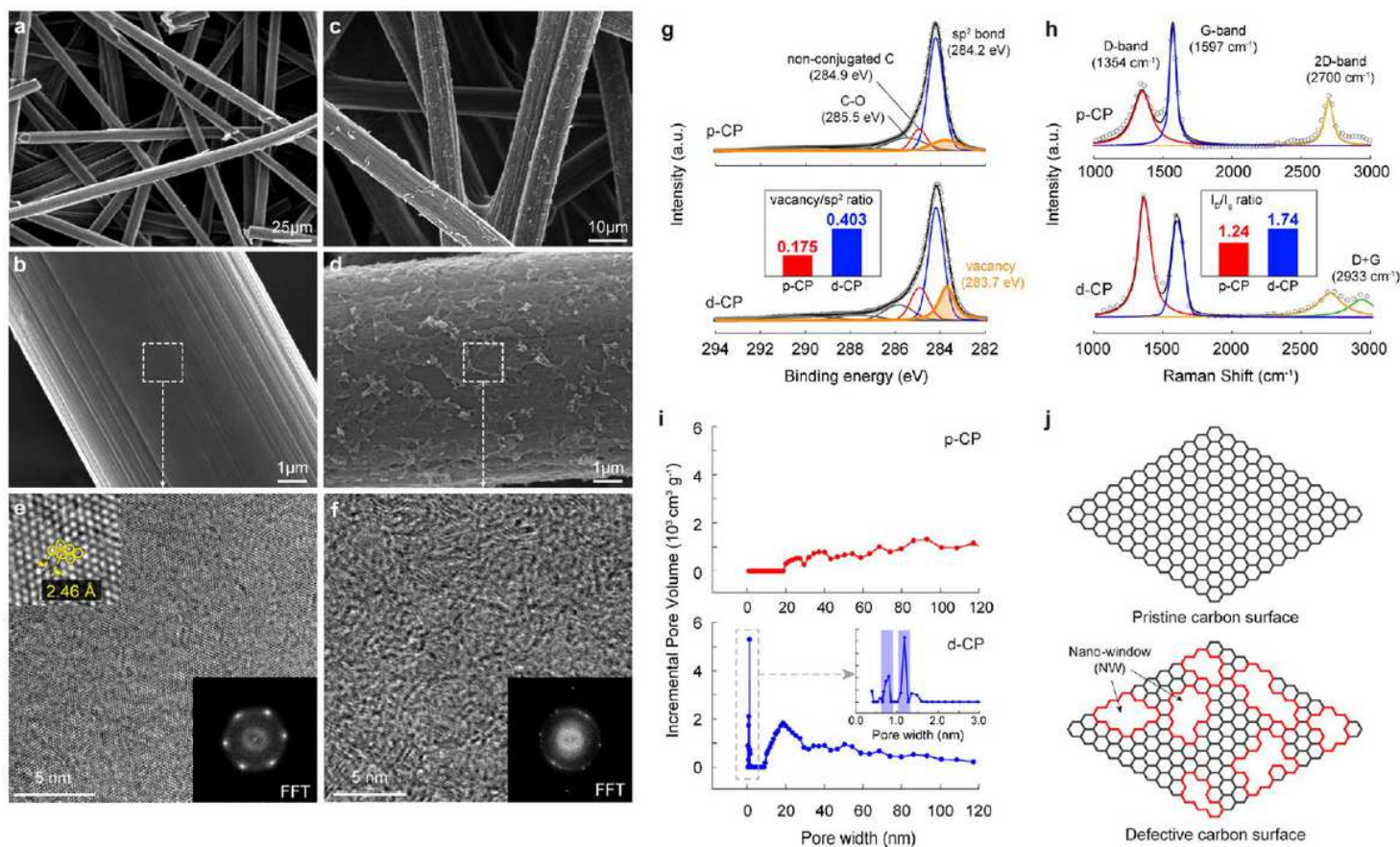


Figure 2

Atomistic structure of the defective carbon layer. a-d, SEM images of p-CP (a, b) and d-CP (c, d). e, f, HR-TEM images and corresponding FFT patterns for p-CP (e) and d-CP (f). g, C1s HR-XPS spectra for p-CP and d-CP. The binding energy in XPS was calibrated with the C1s sp² peak as 284.2 eV. (Inset: Comparison of the vacancy/sp² ratio determined by dividing the area of the vacancy peak by that of the sp² peak between p-CP and d-CP) h, Raman spectra for p-CP and d-CP. (Inset: Comparison of I_D/I_G ratio calculated by dividing the area of the D-band by that of the G-band between p-CP and d-CP) i, BJH pore size distribution analysis for p-CP and d-CP. Inset is the magnified micropore region for d-CP. j, Schematic illustrations of the atomistic structure of p-CP and d-CP surface. The red line indicates the NW structure of d-CP.

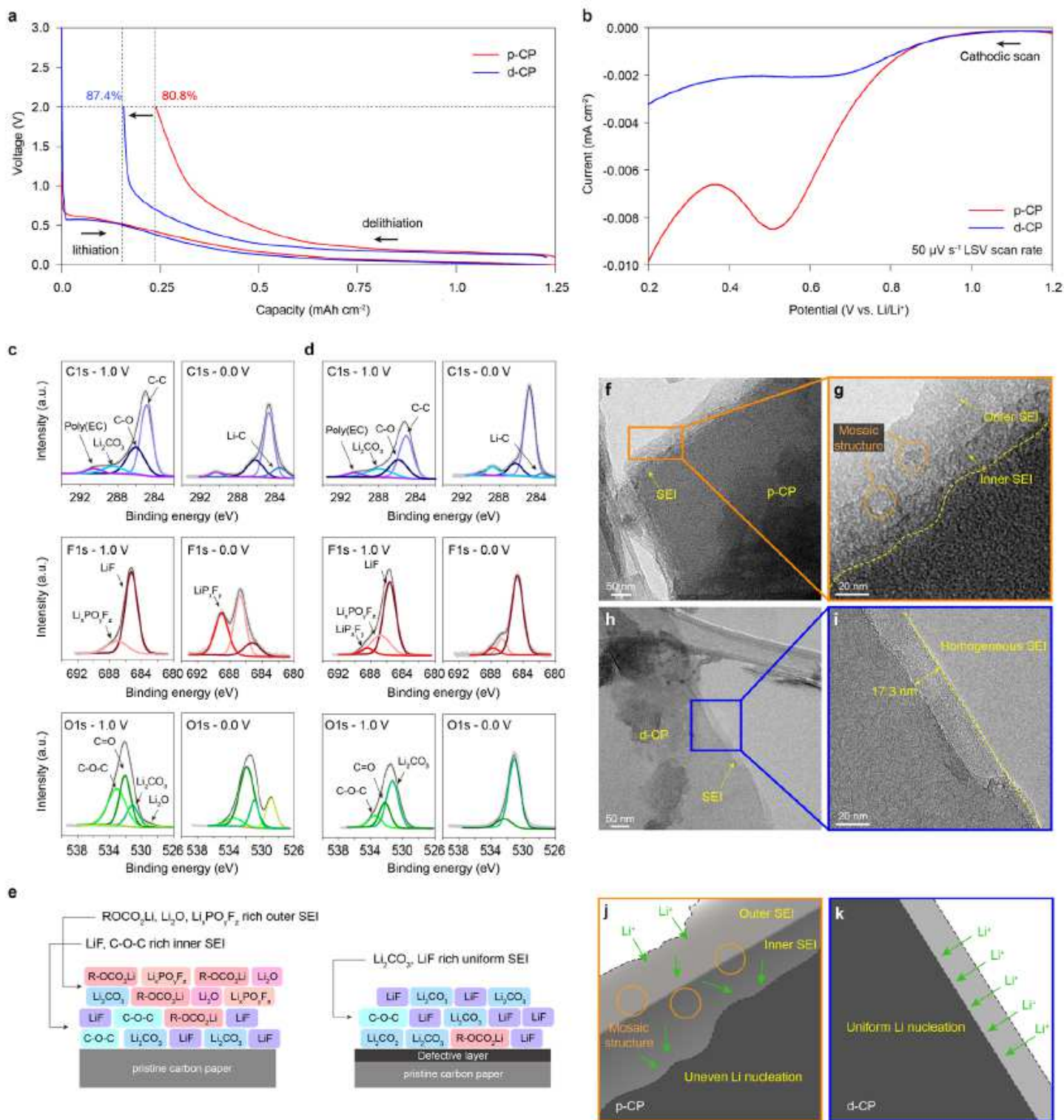


Figure 3

Thin and defect-free SEI formation on the defective layer. a, Galvanostatic lithiation-delithiation curves for Li||p-CP and Li||d-CP cell in the range of 0.0 to 2.0 V at 0.1 mA cm^{-2} for quantification of irreversible capacity at the first cycle due to the electrolyte decomposition at the current collector. b, Current density from electrolyte decomposition based on the active surface area of the current collector (Supplementary Figs. 2a, b) during the LSV measurement (cathodic scan) at $50 \mu\text{V s}^{-1}$ scan rate for Li||p-CP and Li||d-CP

half-cells. c, d, Ex-situ XPS analysis for the SEI layer on p-CP (c) and d-CP (d). The left spectra were taken after galvanostatic reduction at 0.1 mA cm² down to 1.0 V (inner SEI), and the right spectra to 0.0 V (outer SEI). The binding energy was calibrated with the C-C bond peak of 285 eV in C1s spectra. e, Suggested SEI composition on p-CP (left) and d-CP (right). f-i, TEM images of the SEI layers for p-CP (f, g) and d-CP (h, i) after the galvanostatic reduction to 0.0 V j, k, Schematic representation of the microstructure of SEI formed on p-CP (j) and d-CP (k).

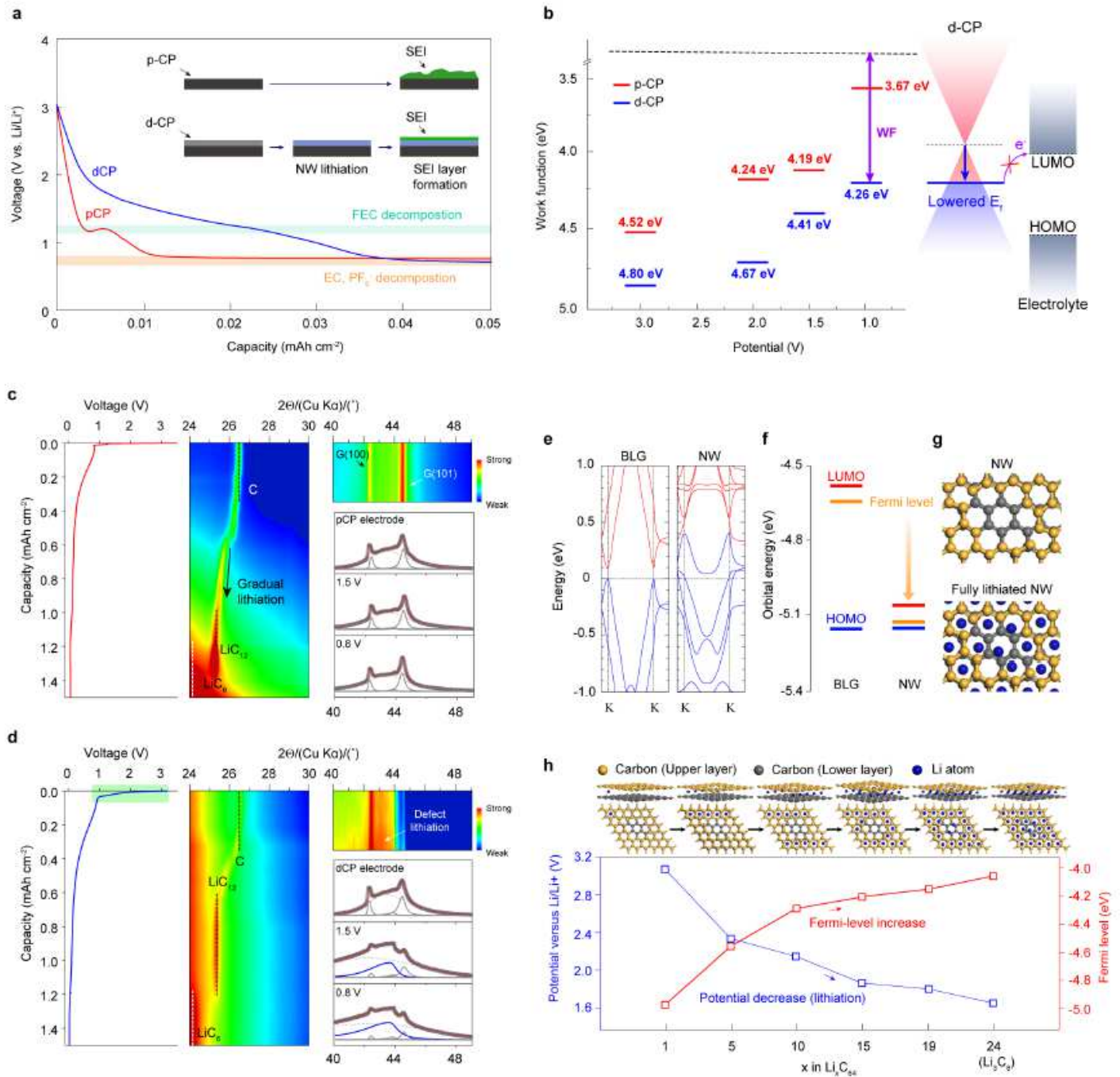


Figure 4

Lithiation of NW structure and electronic property of defect. a, Voltage profile for the early stage of galvanostatic lithiation for p-CP and d-CP at 0.1 mA cm⁻² in half-cell configuration. b, Plots of work

function for p-CP and d-CP as a function of electrode potential from OCV to 1.0 V (V vs. Li/Li+) determined from extrapolation of the secondary cut-off region in UPS (Supplementary Fig. 3). c, d, Image plots of operando XRD spectra along with the potential profile during the first lithiation and deconvoluted XRD patterns at OCV, 1.5 V and 0.8 V for p-CP (c) and d-CP (d). The peaks from the lithiated defect structure (lithiated NW, Li₃C₈) at 43° of 2θ are indicated by blue lines. e, Band structures for perfect BLG and NW defect. The Fermi-level was set to zero. f, Comparison of HOMO, LUMO, and Fermi-level for BLG and NW. g, The relaxed structures of NW and fully lithiated NW (Li₃C₈). The structure of lithiated NW was constructed according to the voltage profiles and XRD spectra. h, DFT calculations of Fermi-level and redox potential for NW at various lithiation degrees. The Li, carbon at the upper layer, and carbon at the lower layer are shown in blue, yellow, and gray color, respectively.

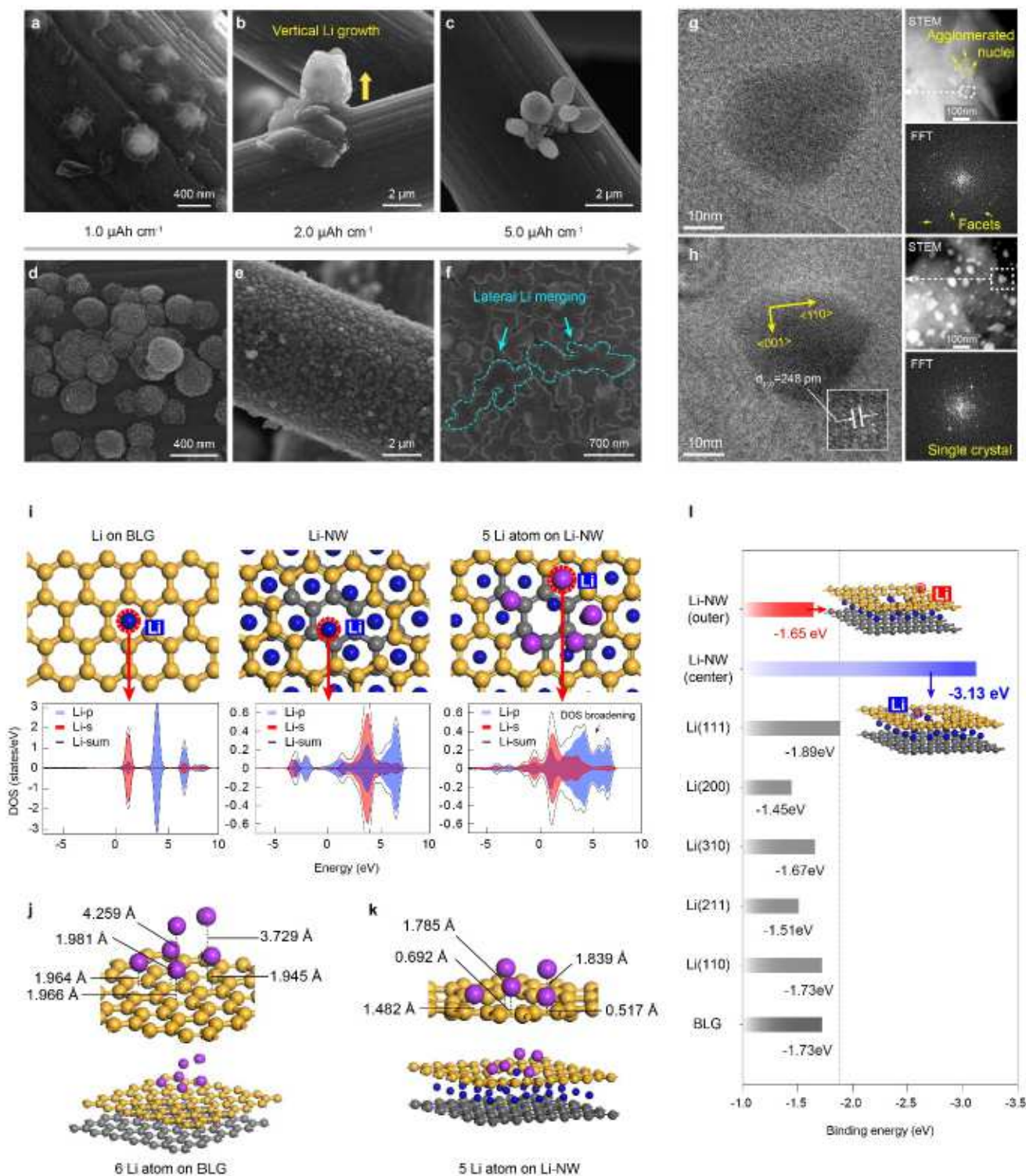


Figure 5

Mechanistic analysis for morphological propensity of Li nucleation and growth on NW structure a-f, SEM images of the Li deposit morphology on p-CP (a-c) and d-CP (d-f) after Li deposition at 1.0 mA cm⁻² for 3.6, 7.2, and 18 s, which correspond to 1, 2, and 5 μAh cm⁻², respectively. g, h, TEM, STEM, and FFT images of Li nuclei on p-CP (g) and d-CP (h) at 1.0 mA cm⁻², 1 μAh cm⁻². i, Relaxed structures and pDOSs of single Li atom adsorbed on perfect BLG, Li-NW, and Li-NW with four pre-adsorbed Li atoms. j, k,

Relaxed configurations of Li atom cluster absorbed on perfect BLG and Li-NW (Li₃C₈). The lithiated Li, Li cluster, carbon at the upper layer, and carbon at the lower layer are shown in blue, purple, yellow, and gray color, respectively. I, Binding energies of Li atom on the outer and center of Li-NW, various facets ((111), (200), (310), (211), (110)) of Li metal, and perfect BLG.

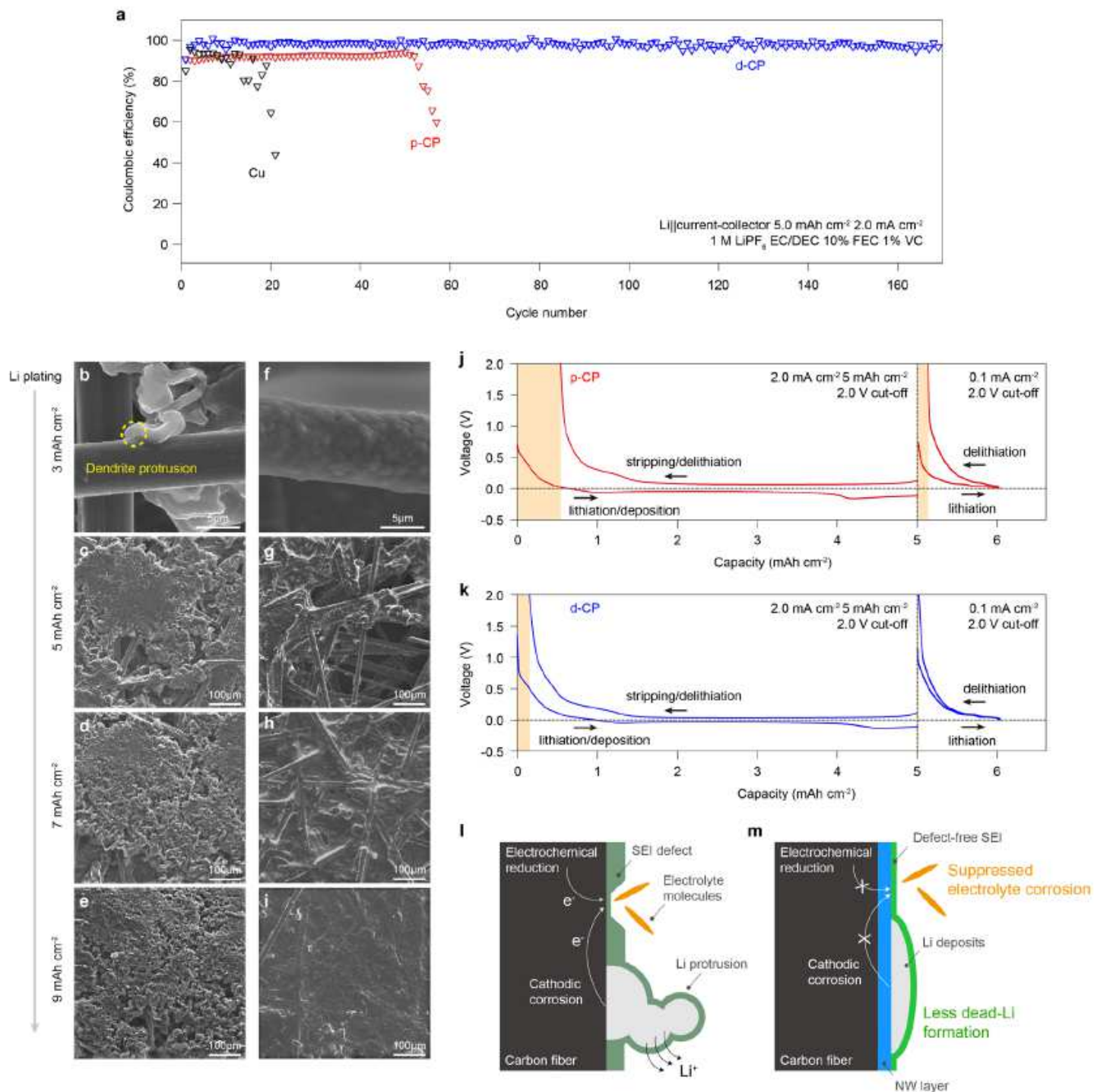


Figure 6

Reversibility of Li plating/stripping on the defective carbon surface. a, The plots of CE as a function of cycle number for Cu, p-CP, and d-CP current collector in half-cell configuration at a current density of 2.0

mA cm⁻² and a capacity of 5.0 mAh cm⁻². b-i, Li deposition morphologies for p-CP (b-e) and d-CP (f-i) at various plating capacities from 3.0 to 9.0 mAh cm⁻². j, k, Quantification of irreversible capacity derived by Li metal plating/stripping and sequential restoration of damaged SEI on current collector surface. The restoration of SEI was performed by galvanostatic cycling with voltage cut-off of 0 V to 2.0 V at a current density of 0.1 mA cm⁻². l, m, Schematics for the irreversible loss of Li and the electrolyte on p-CP surface (l), and the proposed mechanism for prevention of the irreversibility on d-CP surface (m).

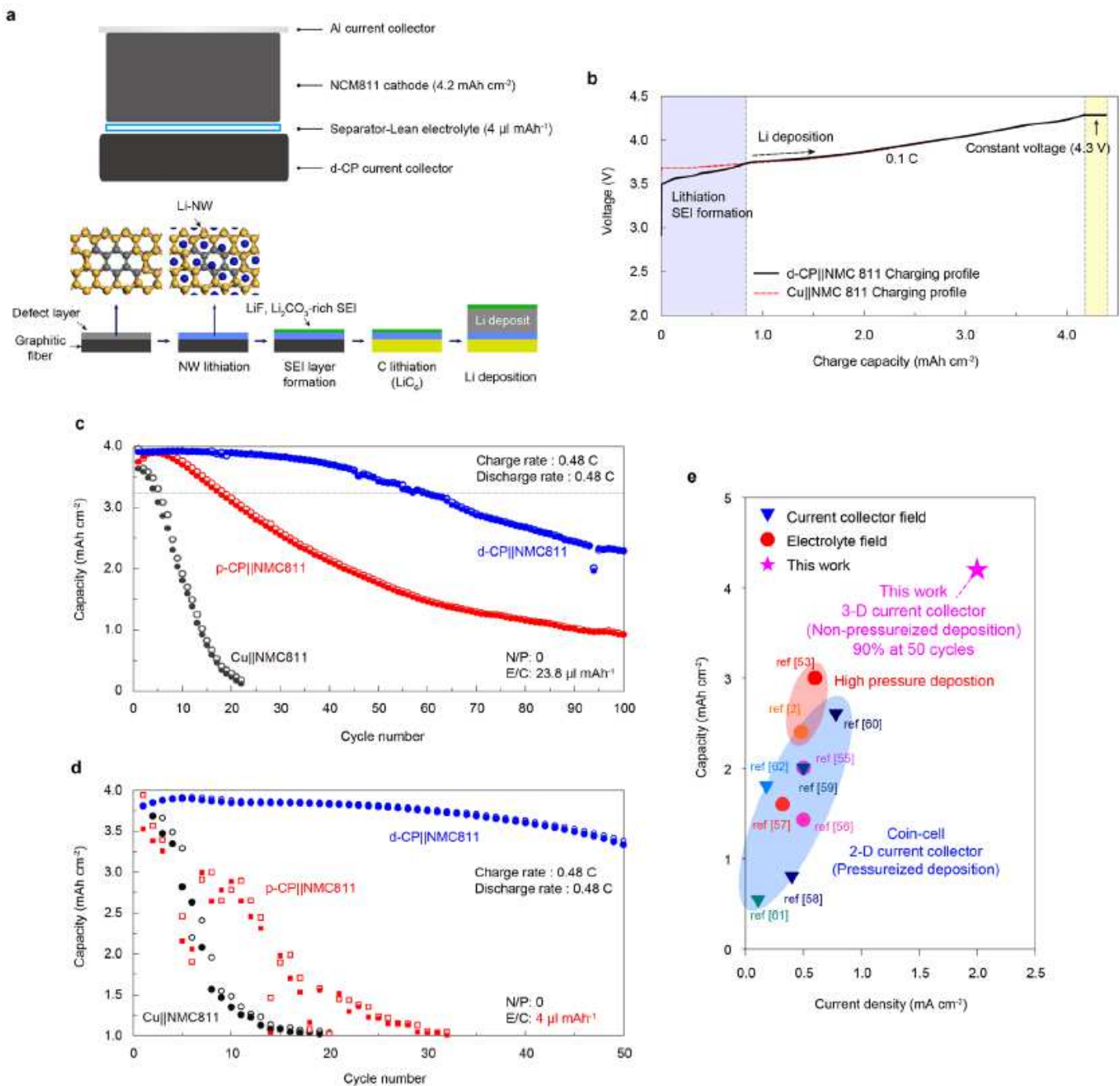


Figure 7

Electrochemical performance of AF-LMB with d-CP under realistic conditions. a, Configuration of anode-free cells with d-CP and high loading (4.2 mAh cm^{-2}) NCM811 cathode; evolution of the anode structure during the first charging. b, Voltage profiles of the AF- NCM811 full cell with Cu or d-CP during the charging at 0.1 C and sequential constant voltage charging at 4.3 V (cut-off current: 0.02 C). c, d, The plots of discharge (filled symbols) and charge (open symbols) capacities as a function of cycle number for the AF-NCM811 full cells with $1 \text{ M LiPF}_6 \text{ EC/DEC } 10\% \text{ FEC } 1\% \text{ VC}$ in a flooded cell condition (c) (E/C ratio of $23.8 \text{ } \mu\text{l mAh}^{-1}$) and a lean electrolyte condition (d) (E/C ratio of $4.0 \text{ } \mu\text{l mAh}^{-1}$). The flooded and lean electrolyte cells were cycled at a charge/discharge rate of 0.48 C (2 mA cm^{-2}) with a potential window of $2.7\text{-}4.3 \text{ V}$. e, Comparison of the areal capacity and current density ensuring stable operation for this work and previous works.

Supplementary Files

This is a list of supplementary files associated with this preprint. Click to download.

- [SupplementaryInformation.pdf](#)